

1 **A vorticity-divergence view of internal wave generation**  
2 **by tropical cyclones: insights from Super Typhoon**  
3 **Mangkhut**

4 **Noel G. Brizuela<sup>1</sup>, T. M. Shaun Johnston<sup>1</sup>, Matthew H. Alford<sup>1</sup>, Olivier**  
5 **Asselin<sup>1</sup>, Daniel L. Rudnick<sup>1</sup>, James N. Moum<sup>2</sup>, Elizabeth J. Thompson<sup>3</sup>,**  
6 **Shuguang Wang<sup>4</sup>, Chia-Ying Lee<sup>5</sup>**

7 <sup>1</sup>Scripps Institution of Oceanography, University of California, San Diego, La Jolla, CA, USA

8 <sup>2</sup>College of Earth, Ocean and Atmospheric Science, Oregon State University, Corvallis, OR, USA

9 <sup>3</sup>NOAA Physical Sciences Laboratory, Boulder, CO, USA

10 <sup>4</sup>School of Atmospheric Sciences, Nanjing University, Nanjing 210023, China

11 <sup>5</sup>Lamont-Doherty Earth Observatory, Columbia University, New York, NY, USA

12 **Key Points:**

- 13 • Float data, linear theory, and 3D model show that coupling between vorticity and  
14 divergence controls inertial pumping under tropical cyclone
- 15 • Asymmetric sea surface cooling 1.2°C dominated by mixing and modulated by rain-  
16 fall, which used 10% of turbulent energy during forced stage
- 17 • Estimates of turbulent diffusivity explain sea surface cooling rates 0.1 °C hr<sup>-1</sup> un-  
18 der typhoon eye and thermocline mixing in its wake

---

Corresponding author: Noel G. Brizuela, [nogutier@ucsd.edu](mailto:nogutier@ucsd.edu)

**Abstract**

Tropical cyclones (TCs) are powered by heat fluxes across the air-sea interface, which are in turn influenced by subsurface physical processes that can modulate storm intensity. Here, we use data from 6 profiling floats to recreate 3D fields of temperature ( $T$ ), salinity ( $S$ ), and velocity around Super Typhoon Mangkhut (western North Pacific, September 2018). Observational estimates of vorticity ( $\zeta$ ) and divergence ( $\Gamma$ ) agree with output from a 3D coupled model, while their relation to vertical velocities is explained by a linear theoretical statement of inertial pumping. Under this framework, inertial pumping is described as a linear coupling between  $\zeta$  and  $\Gamma$ , whose cycles cause periodic displacements in the ocean thermocline and generate near-inertial waves (NIWs). Vertical profiles of  $T$  and  $S$  show gradual mixing of the upper ocean with diffusivities as high as  $\kappa \sim 10^{-1} \text{ m}^2 \text{ s}^{-1}$ , which caused an asymmetric cold wake of sea surface temperature (SST). We estimate that rain layer destruction used  $\sim 10\%$  of energy used for mixing near the TC track, therefore inhibiting SST cooling. Lastly, watermass transformation analyses suggest that  $\kappa > 3 \times 10^{-3} \text{ m}^2 \text{ s}^{-1}$  above  $\sim 110 \text{ m}$  depth and up to 600 km behind the TC. These analyses provide an observational summary of the ocean response to TCs, demonstrate some advantages of  $\zeta$  and  $\Gamma$  for the study of internal wave fields, and provide conceptual clarity on the mechanisms that lead to NIW generation behind TCs.

**Plain Language Summary**

Near-inertial internal waves (NIWs) are generated by winds and lead to oscillations in the internal structure of ocean currents and stratification. Turbulence induced by the vertical current shear in these waves is key to sustain the upper ocean stratification and circulation. In this study, we use data from 6 autonomous floats deployed ahead of Super Typhoon Mangkhut to reconstruct the ocean's 3D response. Reconstructed velocity fields agree with output from a coupled 3D model. Linear equations for vorticity and divergence are used to explain patterns in measured currents and NIW generation, as inertial coupling between wind-driven vorticity and divergence pumps the stratified ocean interior. Measurements of temperature and salinity detail how turbulent stirring mixed rainfall and thermocline waters into the upper ocean. Our analyses indicate that turbulent mixing rates are greatest within 100 km of the typhoon eye but remain elevated hundreds of kilometers behind Mangkhut. Theory and observations presented here provide a comprehensive view of the ocean response to fast-moving, high-intensity tropical cyclones.

**1 Introduction**

Wind-powered currents that rotate near the inertial frequency ( $f$ ) dominate upper ocean dynamics behind fast-moving tropical cyclones (TCs). On the right (left) side of Northern (Southern) hemisphere storms, transient winds amplify the magnitude of inertial currents, but suppress them on the opposite side (Chang & Anthes, 1978; Price, 1981). Horizontal convergence and divergence associated with these currents lead to inertial pumping of the mixed layer (ML) base. This process transfers ML momentum into near-inertial internal waves (NIWs) that later propagate across the ML base and into the thermocline (Price, 1983; Gill, 1984; D'Asaro et al., 2007; Sanford et al., 2011; Johnston et al., 2021). Although inertial pumping and its interactions with background ocean motions are well understood (Balmforth et al., 1998; Whitt & Thomas, 2015; Thomas et al., 2020), general approaches that help understand links between storm morphology and resulting patterns of NIW generation are still lacking.

Turbulence and advection associated with near-inertial motions help redistribute heat across subsurface reservoirs. Notably, shear-driven turbulence at the ML base cools

68 the sea surface temperature (SST) during and shortly after TC passage, reducing sub-  
 69 sequent heat fluxes to the atmosphere and helping modulate storm intensity (Emanuel,  
 70 1999; Glenn et al., 2016). Although SST cooling by turbulent mixing typically stops af-  
 71 ter TC passage, the subsurface effects of mixing in TC wakes over longer timescales re-  
 72 main unclear. However, the final vertical distribution of temperature anomalies that re-  
 73 sult from this mixing determines a TC’s impact on ocean heat uptake and transport (Jansen  
 74 et al., 2010). Therefore, in situ measurements are necessary to estimate the magnitude  
 75 of  $\kappa$  in TC wakes and assess the reliability of SST-based parameterizations of TC-driven  
 76 mixing (Srifer & Huber, 2007; Korty et al., 2008).

77 In this article, we use data from six profiling floats (Johnston et al., 2020, 2021)  
 78 to reconstruct the 3D fields of temperature ( $T$ ), salinity ( $S$ ), and currents ( $u, v, w$ ) be-  
 79 neath Super Typhoon Mangkhut (Fig. 1). Our treatment of the data is validated using  
 80 output from a coupled 3D ocean-atmosphere model of Mangkhut. Under the assump-  
 81 tion that the upper ocean response to TC forcing approaches a steady state when viewed  
 82 in storm-following coordinates (Geisler, 1970), we diagnose the roles of upwelling, ad-  
 83 vection, and mixing in the redistribution of subsurface heat and rainfall inputs. Float  
 84 velocity data are used to validate linear theory results showing that upwelling and NIW  
 85 generation under TCs result from the coupling of ML vorticity ( $\zeta \equiv \frac{\partial v}{\partial x} - \frac{\partial u}{\partial y}$ ) and di-  
 86 vergence ( $\Gamma \equiv \frac{\partial u}{\partial x} + \frac{\partial v}{\partial y}$ ) by Earth’s rotation. As explained below, this coupling is equiv-  
 87 alent to the horizontal rotation of near-inertial currents.

88 Section 2 describes our data and processing methods including details about the  
 89 3D model used for validation. Section 3 lays out the linear theory of upwelling and NIW  
 90 generation under TCs and reformulates standard ML dynamics in terms of  $\zeta$  and  $\Gamma$  to  
 91 demonstrate their inertial coupling. Section 4 presents observational and modelled maps  
 92 of  $(u, v)$  to verify relations between wind forcing, vorticity, divergence and NIW gener-  
 93 ation. Indirect evidence of turbulent mixing under Mangkhut is presented using float mea-  
 94 surements of  $T$  and  $S$  in Section 5. A discussion of our methods and results is presented  
 95 in Section 6, while conclusions are given in Section 7.

## 96 2 Data and Methods

97 Super Typhoon Mangkhut originated on September 7, 2018 as a tropical depres-  
 98 sion in the central Pacific Ocean and later intensified as it moved westwards into the Philip-  
 99 pine Sea. Between September 11 and 15, it sustained maximum 1-minute wind speeds  
 100 above  $70 \text{ m s}^{-1}$ , equivalent to a category 5 hurricane. Throughout this period, SOLO-  
 101 II floats (Davis et al., 2001) sampled the ocean response under the TC (Fig. 1b). The  
 102 combination of Mangkhut’s long lifespan and elevated intensity put it among the 0.5%  
 103 most powerful tropical storms on record (Fig. 1c, Emanuel 2005). As it travelled through  
 104 the Philippine and South China Seas, Mangkhut caused significant damage and loss of  
 105 life in the Philippines, Guam, Taiwan, Hong Kong, and China (Wamsley, 2018).

106 Upon deployment, the floats modified their buoyancy to dive up to 200 m depth  
 107 and back to the surface at intervals  $< 50$  minutes. While doing so, they upward obtained  
 108 profiles of  $T$  and  $S$ , and drifted westward with the North-Equatorial Current at  $\sim 0.18$   
 109  $\text{m s}^{-1}$  (Fig. 2a, Johnston et al. 2020). Because floats record their coordinates at the be-  
 110 ginning and end of every dive cycle, their Global Positioning System data yields two es-  
 111 timates of horizontal velocity (Fig. 2b).  $\mathbf{u}_{mean}$  is the depth-mean current over the pro-  
 112 filing range and is calculated using the difference between the start and end locations  
 113 of individual dives. Surface estimates  $\mathbf{u}_{surf}$ , which are subject to wave motion and windage,  
 114 are calculated using the drift between consecutive dives, when floats remain at the sur-  
 115 face for  $\sim 5$  minutes while they transfer data via Iridium satellite.

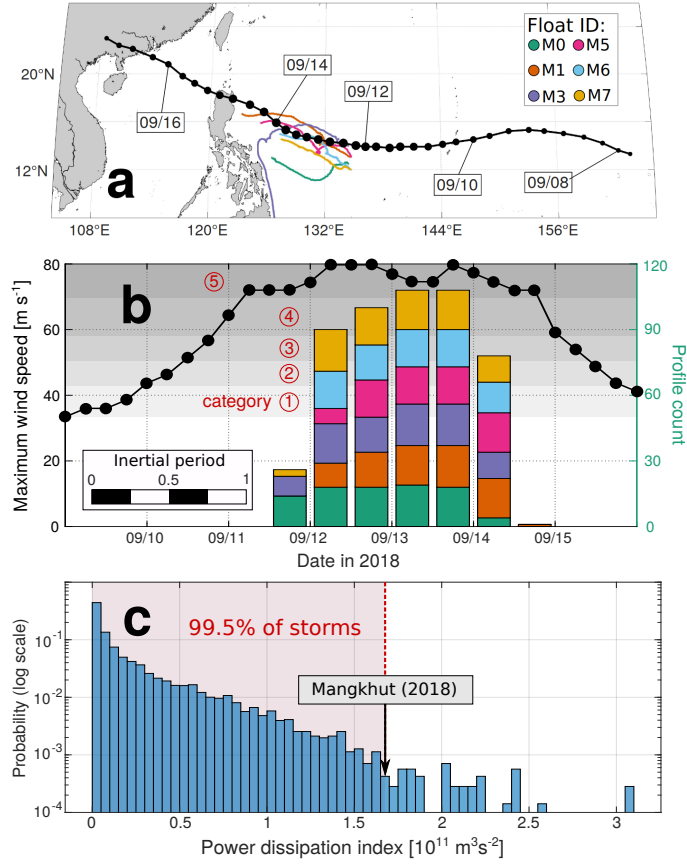


**Figure 1.** TC overview. (a) Best track data from the Joint Typhoon Warning Center shown in black and float trajectories are in colors. (b) Maximum 1-minute sustained wind speed  $|U_{10}|$  (dotted line, left axis) and histogram showing the time distribution of float measurements. Gray shading in shows the wind speed thresholds for Saffir-Simpson TC categories 1 ( $|U_{10}| \leq 30 \text{ m s}^{-1}$ ) to 5 ( $|U_{10}| > 70 \text{ m s}^{-1}$ ). (c) Probability distribution of power dissipation index estimated for  $>7000$  storms puts Mangkhut among the 0.5% most powerful tropical storms in record.

116 Output from a coupled ocean-atmosphere model of Mangkhut is compared to dy-  
 117 namical insights derived from float velocity data. The coupled system uses the Weather  
 118 Research and Forecast (WRF) model V3.8.1 (Skamarock et al., 2008) as its atmospheric  
 119 component, while the ocean is represented by the Hybrid Coordinate Ocean Model V2.2  
 120 (HYCOM; Wallcraft et al. 2009). Horizontal grid spacing in HYCOM was  $1/12^\circ$  for 41  
 121 vertical layers (10 in the upper 50 m) and output was saved at 3 hour intervals. Chen  
 122 & Curcic (2016) give an assessment of this coupled model’s performance under North  
 123 Atlantic TCs. Further details about the model configuration used for Mangkhut were  
 124 given by Johnston et al. (2021).

125 Comparisons of model output against measured  $\mathbf{u}_{surf}$  (Fig. 3) are indicative of both  
 126 the accuracy of the simulation and that of float velocity estimates. Although qualita-  
 127 tive agreement between both datasets is good, neither float nor model data in Fig. 3 should  
 128 be regarded as ground truth for ocean conditions at a time and place. While  $\mathbf{u}_{surf}$  may  
 129 be biased by windage or wave motion, the model’s atmospheric component lets Mangkhut  
 130 evolve dynamically, such that the modelled track and intensity differ slightly from ob-  
 131 servations (Johnston et al., 2021). To account for this, model velocities  $\vec{u}_{hycom}$  in Fig.

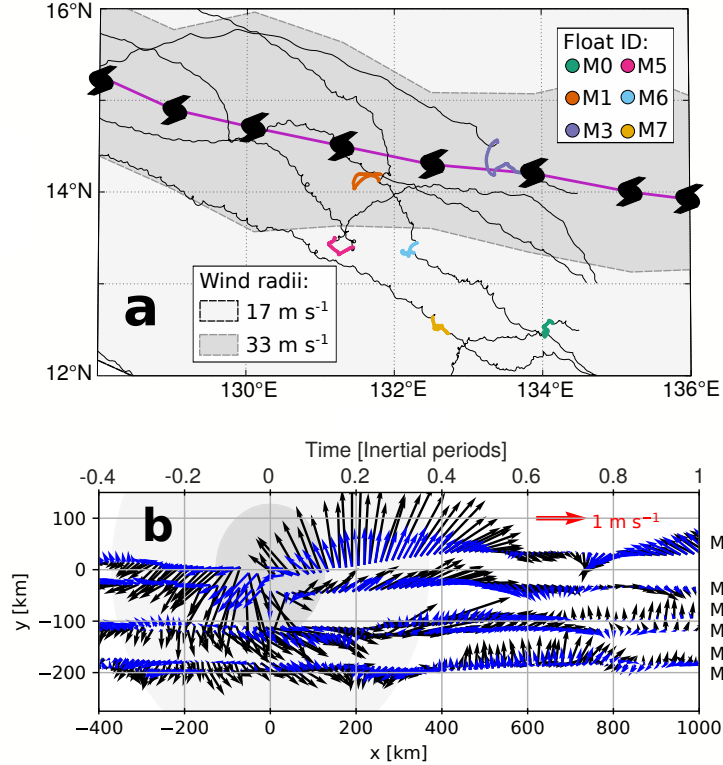


**Figure 2.** (a) 6-hourly JTWC best track data for Mangkhut (light purple). Black lines mark float trajectories, while the locations of vertical profiles used in this study are highlighted in colors. (b) Plane view of  $\mathbf{u}_{surf}$  (black) and  $\mathbf{u}_{mean}$  (blue), with  $x$  and  $y$  components scaled equally to show the true direction of currents in storm-following coordinates  $(x, y)$ .

3 were taken from the average location of each float within 24 h of TC passage. As described next, objective mapping of float data onto storm-following coordinates provides a more meaningful representation of ML dynamics under Mangkhut than pointwise comparisons in Fig. 3.

### 2.1 3D reconstruction of the ocean response

Best track data for Mangkhut from the Joint Typhoon Warning Center (JTWC) was linearly interpolated to the times of float data, which were then reorganized in storm-following coordinates  $(x, y)$  (Fig. 2b). Positive values of  $x$  denote regions behind the storm eye, while  $y > 0$  indicates locations right of the TC track. Likewise,  $\mathbf{u}_{surf}$  and  $\mathbf{u}_{mean}$  were rotated such that  $u$  and  $v$  represent along-track and cross-track velocities respectively. Plots in  $(x, y)$  use the equivalent time  $t = x/U_{storm}$  ( $U_{storm} = 6.2 \text{ m s}^{-1}$ ) to preserve information about temporal variability that has been mapped onto  $x$ . Time scaling  $t \frac{f}{2\pi}$  uses the inertial period  $\frac{2\pi}{f}$  at 15.54°N ( $\sim 45 \text{ hr}$ ) such that one inertial period in  $t$  corresponds to  $U_{storm} \frac{2\pi}{f} = 1000 \text{ km}$  in  $x$  (Fig. 2b).

Despite the fact that each float effectively sampled different parts of the storm at different times (Fig. 2a), both  $\mathbf{u}_{surf}$  and  $\mathbf{u}_{mean}$  line up with  $v < 0$  ( $v > 0$ ) for  $x < 0$  ( $x > 0$ ) and later rotate in the clockwise sense in the TC wake. Such similarities in measurements made by different floats at different times in Fig. 2b suggest that the ocean response was steady within the TC-following  $(x, y)$  coordinates (Geisler, 1970). To best

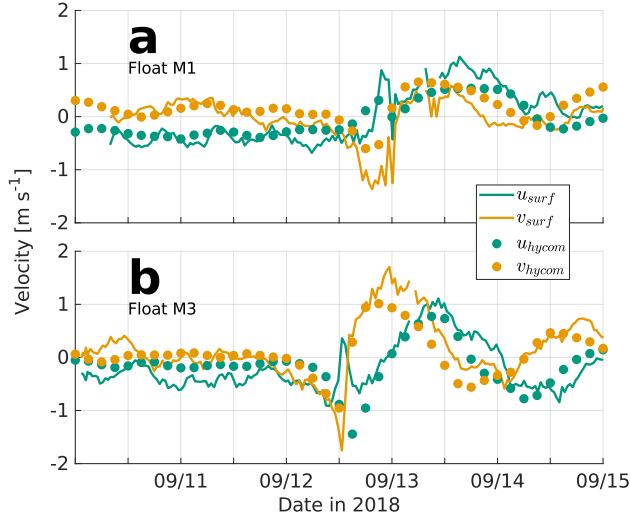


**Figure 3.** Model-observation comparison of upper ocean velocities. ML velocities  $\vec{u}_{hycom}$  (circles) at fixed locations in the coupled 3D model are compared against measurements  $\vec{u}_{surf}$  (solid lines) from floats (a) M1 and (b) M3.

151 exploit the spatiotemporal information embedded in float data, we used objective map-  
 152 ping (Davis, 1985; Le Traon et al., 1998) with a Gaussian decorrelation scale of 150 km  
 153 to horizontally interpolate measurements  $\mathbf{u}_{surf}$ ,  $\mathbf{u}_{mean}$ ,  $T$ , and  $S$ . The signal-to-noise  
 154 ratio for objective mapping was set to 10, and areas where the estimated mean square  
 155 error of interpolated fields is greater than 7.5% of signal variance have been masked out  
 156 in plots.

157 To reconstruct 3D patterns in  $T$  and  $S$ , we stacked 2D maps at 5 m intervals, thus  
 158 producing  $T^*(x, y, z)$  and  $S^*(x, y, z)$ . Here, the star \* denotes objectively mapped vari-  
 159 ables. Although vertical variations in  $u, v$  were not measured directly, we use differences  
 160 between  $\mathbf{u}_{surf}^*$  and  $\mathbf{u}_{mean}^*$  to separate the ML flow from the less energetic ocean below  
 161 (Johnston et al., 2021). More precisely, we assume that depth-dependence at each lo-  
 162 cation  $(x, y)$  is given by

$$163 \quad \mathbf{u}^*(x, y, z) = \begin{cases} \mathbf{u}_{surf}^* & z \geq -h \\ \mathbf{u}_{surf}^* + \left\langle \frac{\partial \mathbf{u}}{\partial z} \right\rangle (z - h) & -h > z > -h - l \\ \mathbf{u}_{surf}^* + \left\langle \frac{\partial \mathbf{u}}{\partial z} \right\rangle l & -h - l \geq z \geq -H. \end{cases} \quad (1)$$

164 The piecewise function (1) includes two layers of depth-constant velocity and a sheared  
 165 transition layer between them. Flow in the uppermost layer, which spans the depth of  
 166 the ML  $-h < z \leq 0$ , is given by  $\mathbf{u}_{surf}^*$ . Here,  $h$  is defined as the depth at which  $T^*$   
 167 is  $0.2^\circ\text{C}$  colder than it is at 20 m depth; this helps avoid transient effects of diurnal warm  
 168 layers and rain layers, whose timescale of dynamical significance under intense wind forc-  
 169 ing is much shorter than that of near-inertial motions (E. J. Thompson et al., 2019; Hughes  
 170 et al., 2020). Below  $z = -h$ , we assume a transition layer of thickness  $l$  and constant  
 171 shear

$$\left\langle \frac{\partial \mathbf{u}}{\partial z} \right\rangle = 2H \frac{\mathbf{u}_{surf}^* - \mathbf{u}_{mean}^*}{[l^2 + 2l(H - l - h)]}. \quad (2)$$

172 This transition layer is set by the vertical penetration of wind-driven turbulent mo-  
 173 mentum, which determines the depth at which  $\mathbf{u}$  no longer behaves like a slab (Turner  
 174 & Kraus, 1967; Pollard et al., 1973). In reality, the transition layer thickness can vary  
 175 considerably and is seen as a stratification and shear maximum below the ML base (John-  
 176 ston & Rudnick, 2009). However, vigorous mixing and internal wave strain behind Mangkhut  
 177 makes it such that a transition layer cannot be reliably identified in profiles of  $T$  and  $S$   
 178 at many locations; therefore, we set a constant thickness  $l = 30$  m. However, Lastly,  
 179 the third and deepest layer extends down to  $H = 180$  m and has velocities  $\mathbf{u}_{surf}^* + \langle \frac{\partial \mathbf{u}}{\partial z} \rangle l$ .  
 180 This construction makes the depth-mean of  $\mathbf{u}^*$  between  $z = 0$  and  $z = -H$  equal to  
 181  $\mathbf{u}_{mean}^*$ .

182 Concentrating  $\langle \frac{\partial \mathbf{u}}{\partial z} \rangle$  within a transition layer captures some of the main features  
 183 of wind-forced currents. Thus, equations (1) and (2) yield an idealized 3D velocity field  
 184 constrained by float velocity estimates and previous knowledge of the baroclinic response  
 185 to TC forcing. However, it should be noted that high baroclinic modes that cannot be  
 186 represented by equation (1).

187 To finalize the reconstruction of 3D flows beneath Mangkhut from float measure-  
 188 ments, we impose a condition of adiabatic continuity to obtain  $\frac{\partial w^*}{\partial z} = -\frac{\partial u^*}{\partial x} - \frac{\partial v^*}{\partial y}$ . Fur-  
 189 thermore, we assume a rigid lid so that  $w^*(z = 0)$  vanishes and the vertical velocity  
 190 is

$$191 \quad w^*(x, y, z) = \int_0^z \left( \frac{\partial u^*}{\partial x} + \frac{\partial v^*}{\partial y} \right) dz'. \quad (3)$$

192 Before showing the interpolated fields  $T^*, S^*, u^*, v^*, w^*$ , we must emphasize that  
 193 (1) the decorrelation scale  $L = 150$  km suppresses high-frequency features in the ob-  
 194 servations, and (2) caution is warranted when interpreting results near the edge of the  
 195 objective maps.

## 196 2.2 Thorpe scale estimates of turbulence

197 Vertical profiles of  $T$  and  $S$  taken at 1 Hz (vertical resolution  $\sim 0.2$  m) were used  
 198 to compute in situ density ( $\rho$ ). These allowed us to derive Thorpe scale estimates (Thorpe,  
 199 1977) of the turbulent dissipation rate ( $\varepsilon$ ) and diffusivity ( $\kappa$ ) within unstable overturns  
 200 where  $\frac{\partial \rho}{\partial z} > 0$ . This method computes the vertical displacements  $d'$  necessary to reorder  
 201 water parcels within a given overturn such that  $\rho$  increases with depth. This defines the  
 202 Thorpe scale as  $L_{Ti} = \sqrt{\langle d'^2 \rangle_i}$ , where the brackets indicate averaging within an over-  
 203 turn  $i$ . Given this,  $\varepsilon$  was calculated as

$$204 \quad \varepsilon_i = 0.64 L_{Ti}^2 \langle N \rangle_i^3. \quad (4)$$

205 Here,  $\langle N \rangle_i$  is the mean buoyancy frequency calculated from the sorted profile of  
 206  $\rho$ . Next, we used the relation in Osborn (1980) to compute  $\kappa_i = 0.2 \frac{\varepsilon_i}{\tilde{N}^2}$ . Here,  $\tilde{N}$  is the  
 207 background buoyancy frequency from sorted profiles of  $\rho$ . With this,  $\varepsilon$  and  $\kappa$  were in-  
 208 directly estimated for all overturns whose  $L_{Ti} > 5$  m. This allows us to estimate the  
 downward turbulent heat flux

$$209 \quad J_{qi} = \rho_0 C_p \kappa_i \left\langle \frac{\partial T}{\partial z} \right\rangle_i. \quad (5)$$

210 Here, the constants are  $\rho_0 = 1024$  kg m $^{-3}$  and  $C_p = 4000$  J kg $^{-1}$  °C $^{-1}$ . More  
 211 details on the implementation, assumptions, and limitations of the Thorpe scale method  
 212 can be found in Johnson & Garrett (2004); A. Thompson et al. (2007); Mater et al. (2015);  
 Scotti (2015).

### 213 3 Mixed layer theory

214 In this section, we review the mechanisms of NIW generation by TCs and formu-  
 215 late linear ML dynamics. Instead of understanding ML motions using depth-averaged  
 216 ML currents  $\bar{\mathbf{u}} = (\bar{u}, \bar{v})$ , we use their vorticity ( $\zeta = \nabla \times \bar{\mathbf{u}}$ ) and divergence ( $\Gamma = \nabla \cdot \bar{\mathbf{u}}$ ).  
 217 This change of variables leads to a coupling between  $\zeta$  and  $\Gamma$  that gives rise to inertial  
 218 pumping and helps conceptualize NIW generation by TCs as a 1D rather than 3D pro-  
 219 cess. By stating inertial pumping as a set of ordinary differential equations rather than  
 220 partial, as done by Gill (1984), the spatiotemporal patterns of NIW generation are more  
 221 easily related to the morphology of atmospheric forcing  $\tau = (\tau_x, \tau_y)$ .

222 The response of  $\bar{\mathbf{u}}$  to  $\tau$  in a ML of thickness  $h$  can be described using the linear slab  
 223 model

$$\frac{\partial \bar{u}}{\partial t} = f\bar{v} + \frac{\tau_x}{\rho_0 h} - r\bar{u} \quad (6)$$

$$\frac{\partial \bar{v}}{\partial t} = -f\bar{u} + \frac{\tau_y}{\rho_0 h} - r\bar{v} \quad (7)$$

$$\frac{\partial h}{\partial t} + h\nabla \cdot \bar{\mathbf{u}} = W_e \quad (8)$$

224 Solutions to these equations, first used by Pollard & Millard (1970) to explain in  
 225 situ measurements of  $\bar{\mathbf{u}}$ , feature a slowly-varying component that approximates an Ek-  
 226 man balance and inertial oscillations whose amplitude decays according to a damping  
 227 coefficient ( $r$ ). In order to resolve vertical velocities ( $\frac{\partial h}{\partial t}$ ) at the ML base, we couple (6)  
 228 and (7) to the continuity equation (8). Here,  $W_e \geq 0$  is an entrainment rate used to  
 229 represent ML deepening caused by turbulent mixing (Price, 1981).

230 Because our focus here is on NIW generation, equations (6)-(8) exclude forces that  
 231 make negligible or secondary contributions to  $\frac{\partial h}{\partial t}$ . For example, barotropic flows develop  
 232 in TC wakes (Shay & Chang, 1997), but the horizontal pressure gradients that drive them  
 233 scale to make a negligible contribution to  $\frac{\partial h}{\partial t}$  in baroclinic modes under TCs (Geisler,  
 234 1970; Gill, 1984; D'Asaro, 1989). Equations (6) and (7) ignore horizontal pressure gra-  
 235 dients that result from gradients in both surface elevation and ML density. Similarly, so-  
 236 lutions of  $\frac{\partial h}{\partial t}$  that account for advective terms  $\bar{\mathbf{u}} \cdot \nabla \bar{\mathbf{u}}$  and  $\bar{\mathbf{u}} \cdot \nabla h$  under TCs (Price, 1981)  
 237 show good agreement with the linear case solved by Geisler (1970), so the advective terms  
 238 can be dropped.

239 When the ML base oscillates at frequencies slightly greater than  $f$ , periodic pump-  
 240 ing of the ML base allows downward momentum transfer by NIWs (Price, 1983; Gill, 1984).  
 241 The full baroclinic ocean response to TCs must be represented by coupling contiguous  
 242 layers of increasing density through pressure gradients produced by interfacial displace-  
 243 ments (Geisler, 1970; Price, 1983). Given that their focus is on the ML, equations (6)  
 244 and (7) do not represent these thermocline processes explicitly. Rather, they use the em-  
 245 pirical damping rate  $r$  to parameterize the gradual decay of ML momentum that results  
 246 from them (Pollard & Millard, 1970; D'Asaro, 1989; D'Asaro et al., 1995).

247 The value of  $r$  is typically determined empirically to fit observations of  $\bar{\mathbf{u}}$  (Pollard  
 248 & Millard, 1970; Alford & Gregg, 2001; Guan et al., 2014), but is meant to represent the  
 249 effects of internal wave propagation, nonlinearities, and turbulent dissipation alike. Pre-  
 250 vious studies have sought to derive scalings of the type  $r^{-1} \sim E_{NIW}/F_{NIW}$ , where  $E_{NIW}$   
 251 is the near-inertial energy and  $F_{NIW}$  is the corresponding energy flux (Gill, 1984). How-  
 252 ever, such derivations are necessarily incomplete and highly dependent on assumptions  
 253 about the physical process by which NIWs develop horizontal gradients and their cor-  
 254 responding group velocity ( $\mathbf{c}_g$ ). In the mid latitudes, this reduction of horizontal scales

255 is thought to depend on gradients in the mesoscale and planetary vorticity (Kunze, 1985;  
 256 D’Asaro, 1989; Johnston et al., 2016; Asselin & Young, 2020; Thomas et al., 2020). In  
 257 contrast, the spatial structure of TC winds imprints sharp gradients on upper ocean cur-  
 258 rents and thus allows for more rapid generation of NIWs (D’Asaro, 1989). To empha-  
 259 size this point, we now consider the ML response to  $\tau$  not in terms of  $\bar{u}$  and  $\bar{v}$ , but their  
 260 spatial gradients. The final aim here is to elucidate the drivers of inertial pumping in  
 261  $\frac{\partial h}{\partial t}$ , by which NIW energy propagates into the thermocline.

### 262 3.1 Dynamics of wind-forced gradients in the upper ocean

263 Below, we manipulate equations (6)-(8) to isolate the components that contribute  
 264 to  $\frac{\partial h}{\partial t}$  and thus generate NIWs. To do this, we calculate  $\frac{\partial \zeta}{\partial t} = \nabla \times \frac{\partial \bar{\mathbf{u}}}{\partial t}$  and study its  
 265 relation to  $\frac{\partial \Gamma}{\partial t} = \nabla \cdot \frac{\partial \bar{\mathbf{u}}}{\partial t}$ . Taking the curl and divergence of equations (6) and (7) thus  
 266 yields an alternative representation of ML dynamics

$$267 \quad \frac{\partial \zeta}{\partial t} = -f\Gamma + \frac{1}{\rho_0 h} \left( \nabla \times \tau - \frac{\tau}{h} \times \nabla h \right) - r\zeta \quad (9)$$

$$268 \quad \frac{\partial \Gamma}{\partial t} = f\zeta + \frac{1}{\rho_0 h} \left( \nabla \cdot \tau - \frac{\tau}{h} \cdot \nabla h \right) - r\Gamma \quad (10)$$

$$269 \quad \frac{\partial h}{\partial t} + h\Gamma = W_e. \quad (11)$$

270 This formalism does not explicitly include information about the magnitude and  
 271 direction of currents. Instead, it uses the physical principles in equations (6)-(8) to re-  
 272 solve spatiotemporal patterns in  $\frac{\partial h}{\partial t}$  that generate internal waves. While past studies have  
 273 used  $\zeta$  and  $\Gamma$  as the basis of fluid dynamical models (Névir & Sommer, 2009), these vari-  
 274 ables are particularly relevant to NIW generation and their interaction with background  
 275 flows (Gill, 1984; Nagai et al., 2015; Whitt & Thomas, 2015). Furthermore, note that  
 276 under axial-symmetric storms,  $\nabla \cdot \tau$  and  $\nabla \times \tau$  are fully determined by radial and tan-  
 277 gential winds respectively. Thus, equations (9) and (10) show how these separate com-  
 278 ponents of  $\tau$  directly drive orthogonal but coupled modes of motion  $\Gamma$  and  $\zeta$  in the ML.

279 In TC wakes, once winds cease to play a dominant role and the ML evolves freely,  
 280 our diagnostic model (9)-(11) yields the three term balance

$$281 \quad \frac{\partial \zeta}{\partial t} = -f\Gamma - r\zeta \quad (12)$$

$$282 \quad \frac{\partial \Gamma}{\partial t} = f\zeta - r\Gamma. \quad (13)$$

283 This linear system of equations, a damped harmonic oscillator, produces inertial  
 284 cycles in  $\zeta$  and  $\Gamma$  with an exponential decay rate  $r$ . Inertial pumping arises directly from  
 285 these cycles, which are simply a consequence of clockwise rotation in  $\bar{\mathbf{u}}$ . To visualize how  
 286 equations (12) and (13) are an explicit statement of inertial pumping, we follow Gill (1984)  
 287 and set  $\tau = W_e = r = 0$  to consider an initial condition  $(\zeta_i, \Gamma_i) = (c_i, 0)$  at time  $t =$   
 288  $t_i$ , where  $c_i > 0$ . As illustrated in Fig. 4, equations (12) and (13) imply that inertial  
 289 rotation of current vectors transforms  $\zeta$  into  $\Gamma$ , and  $\Gamma$  into  $-\zeta$  at time intervals  $\sim \frac{\pi}{2f}$ .  
 290 Quadrature between  $\zeta$  and  $\Gamma$  in this oscillatory mode means that NIW crests and troughs  
 291 (maximum upward and downward displacements of the ML base) must be surrounded  
 292 by anticyclonic and cyclonic inertial currents respectively (Fig. 4).

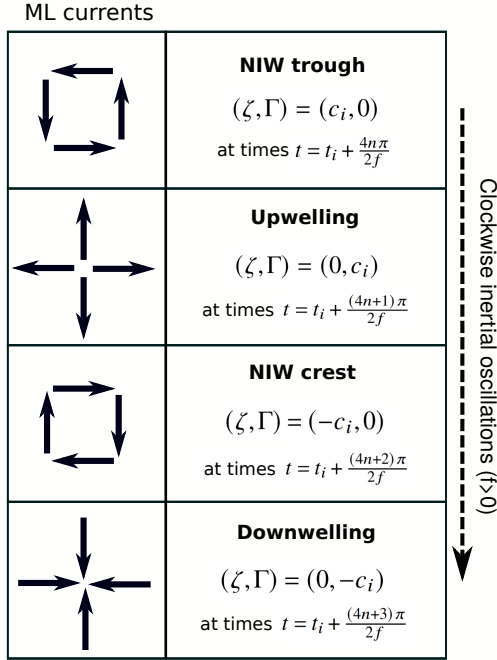


**Figure 4.** Successive rows illustrate the time evolution of current vectors under clockwise inertial oscillations. The left column shows schematic views of  $\mathbf{u}$  at temporal intervals  $\frac{n\pi}{2f}$  ( $n = 0, 1, 2, \dots$ ). Over this period, clockwise rotation of  $\mathbf{u}$  by  $90^\circ$  fully transforms  $\zeta$  into  $\Gamma$ , and  $\Gamma$  into  $-\zeta$ .

293

### 3.2 Relating upwelling and NIW generation to TC winds

294

295

296

297

298

299

300

301

When winds act on the ocean surface, momentum imparted by  $\tau$  drives both mean and turbulent flows. Initially,  $\bar{\mathbf{u}}$  accelerates in the direction of  $\tau$  while turbulence helps distribute momentum vertically and deepen the ML. Later on,  $\bar{\mathbf{u}}$  undergoes inertial rotation and becomes misaligned with  $\tau$ . Variations in the alignment between  $\tau$  and  $\bar{\mathbf{u}}$  play a crucial role in setting the ocean response to TCs. The misalignment gives rise to an asymmetric distribution of ML energy around the TC track (Chang & Anthes, 1978) and can stop ML deepening by turbulence when  $\bar{\mathbf{u}}$  approaches Ekman's balance and the rate of wind work  $\tau \cdot \bar{\mathbf{u}}$  vanishes (Ekman, 1905; Pollard et al., 1973).

302

303

304

305

306

307

Setting  $\nabla h = 0$  in equations (9)-(11), we may write the Ekman balance as  $(\zeta, \Gamma) \sim \frac{1}{f\rho_0 h}(-\nabla \cdot \tau, \nabla \times \tau)$ , so that  $\Gamma$  (and the resulting upwelling) is sustained by  $\nabla \times \tau$ . However, notice that  $\nabla \times \tau$  does not directly drive the evolution of  $\Gamma$  in equation (10). Instead,  $\frac{\partial \zeta}{\partial t}$  and  $\frac{\partial \Gamma}{\partial t}$  at the initial stages of TC forcing will mirror patterns in  $\nabla \times \tau$  and  $\nabla \cdot \tau$  respectively. It is only later that the inertial rotation of currents gradually links  $\nabla \times \tau$  to  $\Gamma$  and produces upwelling (Fig. 4).

308

309

310

311

312

313

314

315

316

The relative magnitudes of steady (Ekman) and oscillating (NIWs) components of the ocean response to TC forcing is mostly determined by  $U_{storm}$ , the horizontal scale of  $\tau$ , and the group speed of mode-1 internal waves ( $\|\mathbf{c}_g^1\|$ ). Using a two-layer model, Geisler (1970) showed that energy transfer into NIWs decreases with the ratio  $U_{storm}/\|\mathbf{c}_g\|$ , where  $\|\mathbf{c}_g\|$  is the group speed of mode-1 internal waves. At the limit where  $U_{storm}/\|\mathbf{c}_g\| < 1$ , Geisler's solutions predict that the momentum in  $\nabla \times \tau$  is entirely used by Ekman-style upwelling with no oscillatory behavior. Nilsson (1995) later generalized this result by deriving analytical expressions for the power put into geostrophic and NIW modes in a continuously stratified fluid given  $\mathbf{c}_g$ ,  $U_{storm}$ , and the wavenumber spectrum of  $\tau$ .

317 Super Typhoon Mangkhut had  $U_{storm}/c_g \sim 2$ , indicating that the ocean response to  
 318 its forcing may be expected to be dominated by NIWs rather than Ekman-style flows.

319 The formalism in equations (9)-(11) does not explicitly represent  $c_g$ , but instead  
 320 uses  $r$  to parameterize Eulerian momentum decay. Hence, we investigate whether this  
 321 simple model of NIW generation can represent the transition between geostrophic and  
 322 oscillatory regimes described by Geisler (1970) and Nilsson (1995). To do this, we used  
 323 Euler’s method to compute point solutions (setting  $\nabla h = 0$ ) of equations (9)-(11) under  
 324 the forcing of Gaussian vortices  $\nabla \times \tau$  with standard deviations of 2 and 6 hours  
 325 to represent fast- and slow-moving TCs respectively. These vortices represent the chang-  
 326 ing direction of tangential  $\tau$  inside an axisymmetric TC eye but do not include radial  
 327 stresses, which are known to make only minor contributions to NIW generation (Price,  
 328 1983; Shay et al., 1989; Nilsson, 1995). The evolution of  $(\zeta/f, \Gamma/f, h)$  from an initial  
 329 condition  $(0, 0, 80 \text{ m})$  under both forcing scenarios and using  $r = 0.2f$  is shown in Fig. 5.

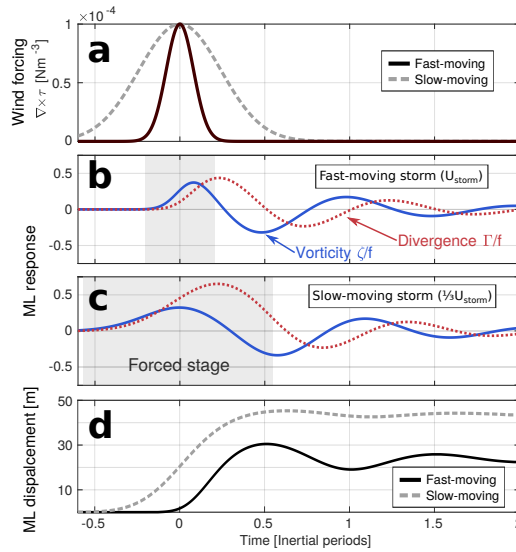


**Figure 5.** ML response (9)-(11) to (a) wind vortices representing (b) a fast-moving TC and (c) one moving at one-third the speed. (d) compares the mixed layer displacements  $h(t_0) - h(t)$  that result from both simulations when  $W_e = 0$  and  $r = 0.2f$ . Gray shading in (b) and (c) marks the forced stage, which is followed by near-inertial pumping as given by (12) and (13).

330 Numerical solutions of (9)-(11) in Fig. 5 exemplify the two fundamental differences  
 331 noted by Geisler (1970). Firstly, notice that the greatest upwelling (maximum  $\Gamma/f$ ) oc-  
 332 curs at the end of the forced stage for the fast-moving case (Fig. 5b), whereas  $\Gamma/f$  peaks  
 333 well within the slow TC’s forced stage (Fig. 5c). Moreover, the net mixed layer displace-  
 334 ment induced by the slow-moving TC is greater than for the fast-moving case (Fig. 5d).

335 The second point of agreement between our simple model and Geisler (1970) re-  
 336 lates to the amplitude of NIWs generated by fast- and slow-moving TCs. While Geisler’s  
 337 analytical solutions to  $\frac{\partial h}{\partial t}$  have no oscillatory behavior when  $\frac{U_{storm}}{c_g} < 1$ ,  $r$  regulates the  
 338 fraction of momentum that enters the damped oscillator in equations (12) and (13) at  
 339 the end of the forced stage. This is evidenced in Fig. 5 because the amplitude of NIWs  
 340 generated by the slow-moving vortex is less than half that NIWs generated in fast-moving  
 341 case (Fig. 5d and Figs. 3-5 in Geisler 1970).

342 The linear  $(\zeta, \Gamma)$  view of ML dynamics (9)-(11) does not include any new physics  
 343 absent from standard ocean models based on  $(u, v)$ . Rather, it uses a simple change of

344 variables to explain inertial pumping (Fig. 4) using ordinary differential equations in-  
 345 stead of partial ones, as done by Gill (1984). This helps conceptualize inertial pumping  
 346 and upwelling as 1D (rather than 3D) processes. Furthermore, coupling between  $\zeta$  and  
 347  $\Gamma$  concretely explains why NIW wakes are generally centered along the TC track where  
 348  $\nabla \times \tau$  peaks and not on its right side, where the greatest concentration of near-inertial  
 349 energy is (Price, 1981, 1983). Namely, NIWs only form where horizontal gradients ( $\zeta$  and  
 350  $\Gamma$ ) exist, and the forcing  $\nabla \times \tau$  that directly drives cycles in  $\zeta$  and  $\Gamma$  is greatest along  
 351 the track. In the next section, we use float measurements and output from WRF-HYCOM  
 352 coupled simulations of Mangkhut ( $U_{storm}/c_g \sim 2$ ) to demonstrate the relevance of (9)-  
 353 (11) in describing NIW generation under fast-moving TCs.

#### 354 4 Upper ocean dynamics beneath Mangkhut

355 We now turn our attention towards model output and observations of upper ocean  
 356 dynamics beneath Super Typhoon Mangkhut. First, we present evidence supporting the  
 357 validity of sampling and interpolation schemes described in Section 2. Second, the evo-  
 358 lution of  $\zeta$  and  $\Gamma$ , and their effect on  $T$  and  $S$  in our observations is explained using nu-  
 359 merical solutions of equations (9)-(11). Altogether, these analyses exemplify and expand  
 360 on the dynamics described in Section 3 and help visualize the mechanisms of NIW gen-  
 361 eration under fast-moving storms. The role of turbulent mixing in changing  $h$  is discussed  
 362 briefly.

363 Mechanisms of NIW generation in model output and observations are compared  
 364 (Fig. 6c) using a time series of the modelled  $(\zeta, \Gamma)/f$  averaged between 14 and 14.5°N  
 365 (solid lines) and float estimates  $\zeta_{surf}^*/f$  along  $y = 0$  (dashed lines). Much like the ide-  
 366 alized solutions in Figs. 4 and 5b, the ML response to Mangkhut can be described as  
 367 a combination of initial forcing by  $\nabla \times \tau$  and later coupling between  $\zeta/f$  and  $\Gamma/f$  by  
 368 inertial rotation of  $\bar{\mathbf{u}}$ . Atmospheric forcing is evidenced by a peak in  $\zeta/f$  under the TC  
 369 eye, while inertial rotation later transformed this response into a peak in  $\Gamma/f$  (Fig. 6c).  
 370 As  $\bar{\mathbf{u}}$  continued to rotate, ML flows reorganized to form minima in  $\zeta/f$  and  $\Gamma/f$  along  
 371 the TC track (Figs. 6a,b). At the end of the first inertial cycle, the ML came to have  
 372  $\zeta/f \approx 0.25$  and  $\Gamma/f \approx 0$  in both the 3D model and observations (Figs. 6c).

373 Broadly speaking, spatial patterns in  $\|\bar{\mathbf{u}}\|$  and  $(\zeta, \Gamma)/f$  in observations (Fig. 7) are  
 374 consistent with those in the 3D model (Fig. 6a,b). Yet, some notable differences between  
 375 the modelled and observed ML response exist. For example,  $\Gamma_{surf}^*/f \sim 0.25$  near the  
 376 leading edge of the TC eye (Fig. 7c), but the 3D model yields  $\Gamma_{hycom}/f \sim -0.1$  there  
 377 (Fig. 6b). Available data is insufficient to reliably attribute such differences to poten-  
 378 tial biases induced by windage and wave motion, our sampling and interpolation scheme,  
 379 or to processes misrepresented in the 3D model. Nevertheless, patterns in  $\mathbf{u}_{surf}^*$  and  $\mathbf{u}_{mean}^*$   
 380 (Fig. 7a,b) are qualitatively similar to each other, suggesting that windage and wave mo-  
 381 tion only had a limited impact on  $\mathbf{u}_{surf}^*$ .

382 With the validity of our observational technique supported by model output, we  
 383 now put our focus on the coupling between  $\zeta/f$  and  $\Gamma/f$  and how it leads to NIW gen-  
 384 eration. To test whether observations are consistent with linear theory, Fig. 8 compares  
 385 interpolated float data along  $y = 0$  to numerical solutions of equations (9)-(11) under  
 386 idealized forcing and with a damping rate  $r = 0.5f$ .

387 Atmospheric forcing  $\nabla \times \tau$  in Fig. 8 corresponds to the reversal of tangential wind  
 388 between opposite sides of the TC eyewall. The magnitude of  $\nabla \times \tau$  used here agrees with  
 389 the mean wind stress curl inside the TC eye ( $\frac{|\tau_{max}|}{MWR} = 2.24 \times 10^{-4} \text{ N m}^{-3}$ , dashed line),  
 390 where  $MWR = 40 \text{ km}$  is the radius of maximum wind and  $|\tau_{max}| = C_D \rho_{air} |U_{10}|^2$  was  
 391 calculated using  $U_{10} = 70 \text{ m s}^{-1}$  (Fig. 1),  $\rho_{air} = 1.22 \text{ kg m}^{-3}$ , and  $C_D = 1.5 \times 10^{-3}$   
 392 (Zweers et al., 2010).

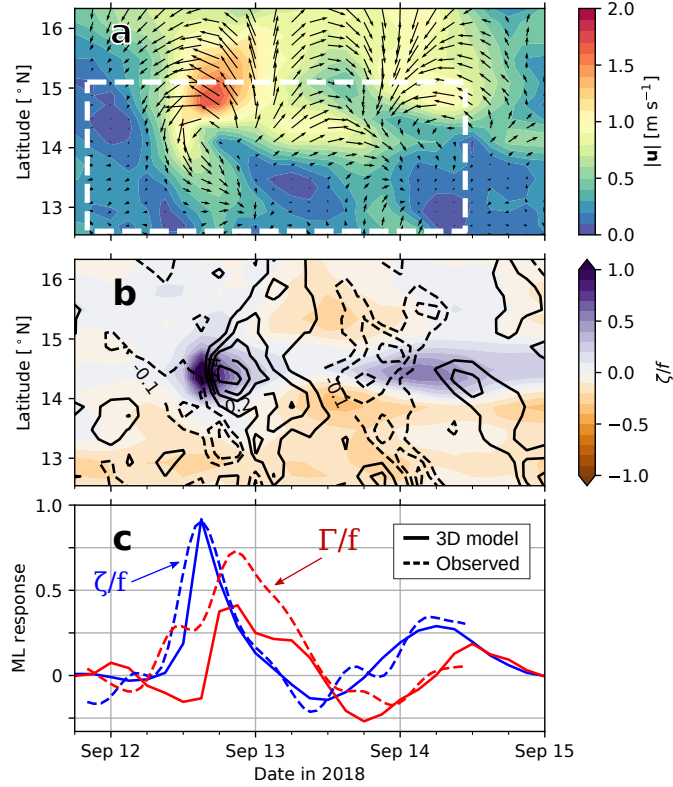


**Figure 6.** Hovmöller diagrams of the ML flow along  $133^\circ\text{E}$  in terms of (a)  $\bar{u}$  and (b)  $(\zeta, \Gamma)/f$  from the 3D coupled model, where black contours denote values  $\Gamma/f = \pm 0.1, 0.2, \dots$  (negative contours dashed). (c) Modelled  $(\zeta, \Gamma)/f$  averaged between  $14$  and  $14.5^\circ\text{N}$  (solid lines) is compared to observed values along  $y = 0$  (dashed lines). The dashed rectangle in panel a is representative of the area and stages of ocean response sampled by floats (Fig. 2b).

393 The magnitude of convergent stresses  $\nabla \cdot \tau < 0$  is set to be artificially low in these  
 394 simulations (Fig. 8a). Although  $\|\nabla \cdot \tau\| \sim \|\nabla \times \tau\|$  in the 3D atmospheric model, the  
 395 response in  $\Gamma$  that is generated by  $\|\nabla \cdot \tau\|$  is rapidly suppressed by 3D and nonlinear  
 396 effects and thus does not contribute significantly to NIW generation in the TC wake (Price,  
 397 1983; Shay et al., 1989). Lastly, it should be noted that forcing in Fig. 8a ignores the  
 398 gradual weakening of  $\tau$  far from the eyewall, where  $\nabla \times \tau < 0$  and  $\nabla \cdot \tau > 0$ .

399 Agreement between linear solutions and observations in Fig. 8 confirms that clock-  
 400 wise rotation of  $\bar{u}$  (Fig. 2b) transformed the wind-forced  $\zeta$  into  $\Gamma$  near the end of the  
 401 forced stage. Momentum in  $\Gamma$  was later transferred to an inertial anticyclone  $\zeta < 0$   
 402 and the cycle continued as shown schematically in Fig. 4. Note that the quality of the fit in  
 403 Fig. 8b is sensitive to various model parameters ( $r$ ,  $\nabla \times \tau$ ,  $\nabla \cdot \tau$ ), and initial conditions  
 404 for  $(\zeta, \Gamma, h)$ . Nonetheless, this analysis confirms that  $\zeta$  and  $\Gamma$  oscillate in quadrature in  
 405 observations, the 3D model, and linear theory (Figs. 6c, 8b). This robust result comes  
 406 from the linear terms by which  $f$  couples  $u$  and  $v$  in equations (6) and (??), and  $\zeta$  and  
 407  $\Gamma$  in equations (9) and (10).

408 When Earth's rotation transferred  $\zeta$  into  $\Gamma$ , the ML base moved upwards and a NIW  
 409 was generated (Figs. 8c, 9a). Observations show that the  $27^\circ\text{C}$  isotherm deepened by  
 410  $\sim 25$  m under the TC eye before it shoaled by 75 m as predicted by linear theory (Fig.  
 411 8c). Initial deepening may be partially explained by turbulent mixing, evidenced by Thorpe

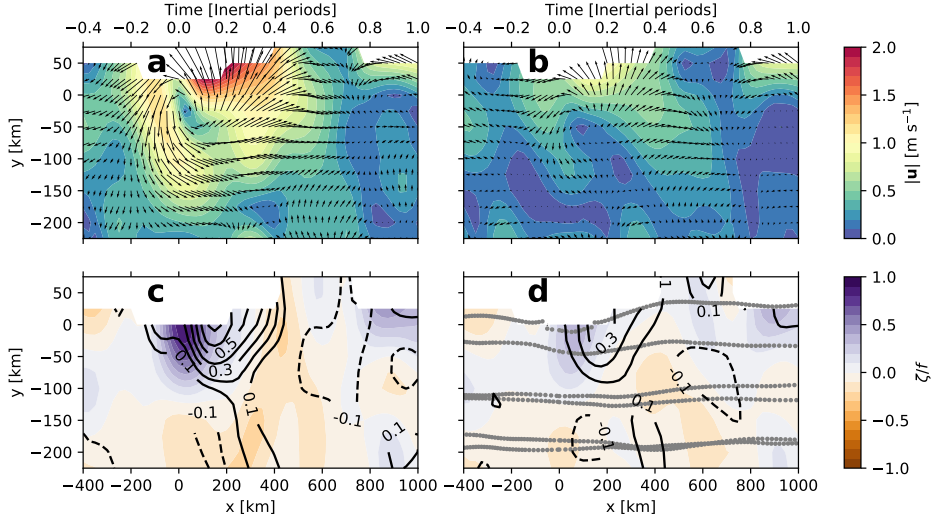


**Figure 7.** Observed ML dynamics under Mangkhut. (a)  $\mathbf{u}_{surf}^*$  and (b)  $\mathbf{u}_{mean}^*$  show current speeds in color shading. (c)  $\zeta_{surf}^*/f$  and  $\Gamma_{surf}^*/f$ , and (d)  $\zeta_{mean}^*/f$  and  $\Gamma_{mean}^*/f$  show the gradient-based description of ML motions. Black solid contours in Figs. 7c,d are for upwelling-favorable values  $\Gamma/f > 0$ , while dashed contours show  $\Gamma/f < 0$ . Dotted lines in Fig. 7d show float trajectories.

412 scale estimates  $\kappa \sim 10^{-1} \text{ m}^2\text{s}^{-1}$  near  $x = 0 \text{ km}$  (Fig. 9b). Agreement between the mod-  
 413 elled  $\frac{\partial h}{\partial t}$  and observed displacements of the  $27^\circ\text{C}$  isotherm behind the TC are consistent  
 414 with  $\Gamma_{surf}^*$  there (Fig. 8c). This result implies that upwelling in the wake of Mangkhut  
 415 resulted from the near-inertial coupling of  $\zeta$  and  $\Gamma$ , marking the generation of a large am-  
 416 plitude NIW. Moreover, the modelled  $\Gamma$  agrees well with  $\Gamma_{surf}^*$  for all  $t > 0$  (Fig. 8b).  
 417 However,  $\Gamma_{surf}^*$  failed to capture downwelling necessary to displace  $h$  after  $t \approx 0.6$  in-  
 418 tertial periods (Fig. 8c).

419 Profiles of  $w^*$  and  $u^*$  in Fig. 9a reveal the structure of upwelling in the wake of Mangkhut.  
 420 There,  $w^*$  reaches  $8 \text{ m h}^{-1}$  and explains isothermal displacements as large as  $75 \text{ m}$  around  
 421  $x = 350 \text{ km}$ .  $T^*$  shows that isotherms had been lifted by  $\sim 20 \text{ m}$  after  $\sim 0.85$  inertial  
 422 periods ( $x = 850 \text{ km}$ , Fig. 9a). This net upwelling is crucial to the process of geostrophic  
 423 adjustment (Geisler, 1970; Nilsson, 1995), and determined in (10)-(11) by the magnitude  
 424 of  $r$ .

425 To test the impacts of advection in setting the ocean stratification behind Mangkhut,  
 426 as well as the accuracy of inferred 3D flows (Eqs. 1-3), the Eulerian heating rate  $\frac{\partial H_c}{\partial t} =$   
 427  $\rho_0 C_p \frac{\partial T^*}{\partial t}$  is calculated along  $y = 0$  through two different methods (Fig. 9b). First, we  
 428 used a frozen field assumption so that  $\frac{\partial T^*}{\partial t} = U_{storm} \frac{\partial T^*}{\partial x}$  (color shading). Second, we  
 429 used  $\mathbf{u}^*$  and  $w^*$  to calculate the advective contribution  $\frac{\partial T^*}{\partial t} \approx -u^* \frac{\partial T^*}{\partial x} - v^* \frac{\partial T^*}{\partial y} - w^* \frac{\partial T^*}{\partial z}$   
 430 (black contours). Note that the latter expression ignores heating by turbulent mixing,  
 431 while the frozen field estimate accounts for all observed heat transfer.

432 Areas of agreement between both estimates of  $\frac{\partial H_c}{\partial t}$  (color shading and black con-  
 433 tours in Fig. 9b) suggest that heat transfer was locally dominated by the vertical ad-  
 434 vection term  $w^* \frac{\partial T^*}{\partial z}$  and that the approximation  $w^*$  is adequate. Similarities are par-  
 435 ticularly good near  $x = 180 \text{ km}$ , where upwelling caused  $\frac{\partial H_c}{\partial t} \sim -500 \text{ W m}^{-3}$ .

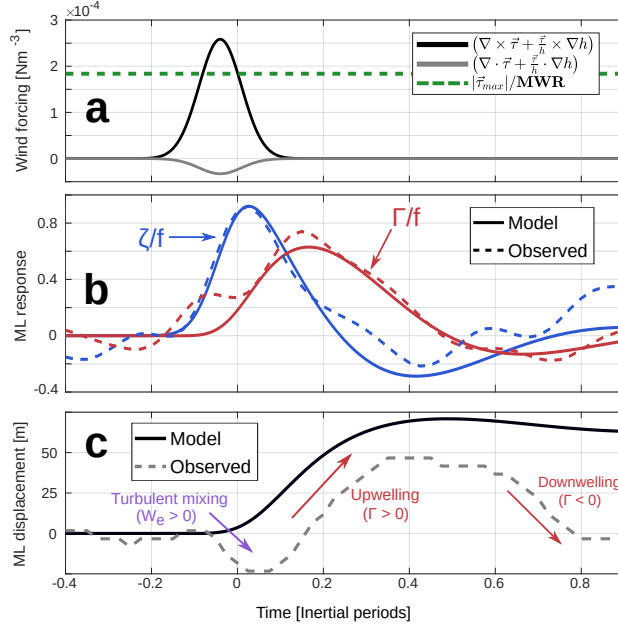


**Figure 8.** ML response to idealized TC-like atmospheric forcing. (a) Idealized wind forcing (solid lines) used to drive the ML linear model in equations (9)- (11) setting  $W_e = \nabla h = 0$  and  $r = 0.5f$ . The dashed green line indicates the mean wind stress curl  $\|\tau_{max}\|/MWR$  of the TC eye. (b) Numerical solutions of  $\zeta/f$  (blue) and  $\Gamma/f$  (red) are compared to observations  $\zeta_{surf}/f$  and  $\Gamma_{surf}/f$  along  $y = 0$  km (Fig. 7c). (c) Linear solutions of  $h(t)$  (solid line) are compared to observed displacements of the  $27^\circ\text{C}$  isotherm (dashed line).

436 Advective estimates of  $\frac{\partial H_c}{\partial t}$  mistakenly predict cooling below 75 m depth around  
 437  $x = 0$ , where  $T^*$  shows heating rates as high as  $300 \text{ W m}^{-3}$  (color shading). Disagree-  
 438 ment between observed heating and advective estimates below the TC eye may be ex-  
 439 plained by a possible bias in  $\Gamma_{surf}^*$  (Fig. 6c) but also by vigorous mixing. Thorpe scale  
 440 estimates  $\kappa \sim 10^{-1} \text{ m}^2 \text{ s}^{-1}$  near  $x = 0$  (Fig. 9b) reveal areas where the correspond-  
 441 ing turbulent heat flux  $J_q \sim 4000 \text{ W m}^{-2}$  could invalidate the assumption that  $\frac{\partial H_c}{\partial t}$   
 442 was dominated by advection. This value of  $J_q$  is roughly 15 times greater than the mean  
 443 daily shortwave flux across the air-sea interface, but transfers heat into the thermocline,  
 444 which is usually not directly impacted by air-sea fluxes.

445 While variations in the ML flow are dominated by near-inertial oscillations (Fig.  
 446 8),  $\frac{\partial H_c}{\partial t}$  also shows the signature of higher-frequency motions (Fig. 9b). Horizontal sec-  
 447 tions of  $\zeta^*/f$ ,  $\Gamma^*/f$ , and  $N^* = \sqrt{-\frac{g}{\rho_0} \frac{\partial \rho^*}{\partial z}}$  at 160 m depth (Fig. 10) feature nearly par-  
 448 allel, periodic stripes that move away from the storm track towards  $y < 0$ . Dashed black  
 449 lines in Fig. 10 help identify this apparent propagation corresponding to a cross-track  
 450 phase speed  $\sim 3.1 \text{ m s}^{-1}$ . While  $\zeta^*/f$  and  $\Gamma^*/f$  are linked by the rotation of current  
 451 vectors (Fig. 4),  $\Gamma^*$  and  $N^*$  are linked by isopycnal displacement and straining. There-  
 452 fore, these three variables offer complementary views of internal wave phase propaga-  
 453 tion.

454 Color shading in Fig. 10c shows the magnitude  $\|\mathbf{u}_{surf}^* - \mathbf{u}_{mean}^*\|$  as a proxy for  
 455 vertical shear below the ML. As evidence of shear instability, Thorpe scale estimates of  
 456  $\varepsilon$  are shown with colored circles (Fig. 10c). Both the greatest  $\varepsilon$  and the greatest den-  
 457 sity of overturns appear within 100 km of the TC eye. Ahead of Mangkhut, overturns

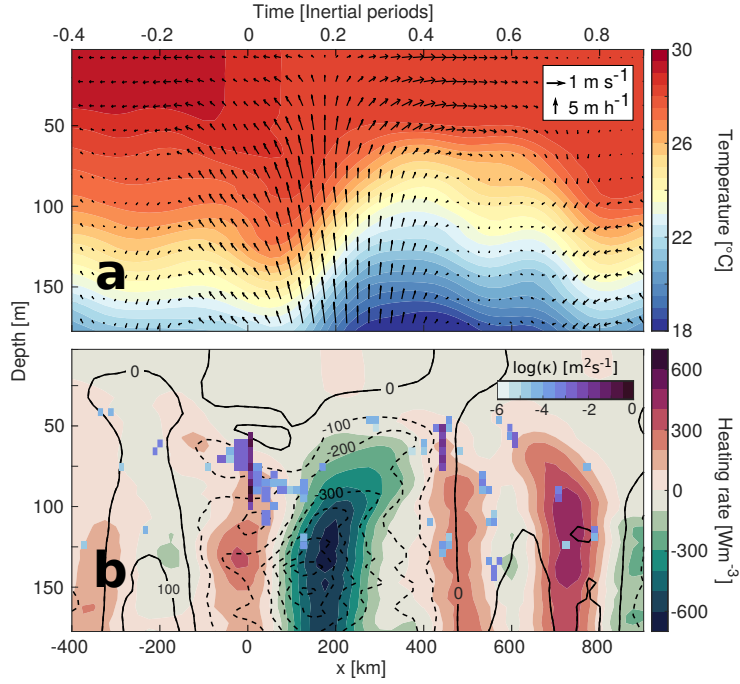


**Figure 9.** (a) Vertical sections of  $T^*$  and  $(u^*, w^*)$  along  $y=0$  show the generation of a NIW behind Super Typhoon Mangkhut. The vertical component  $w^*$  is magnified for clarity. (b) Frozen field estimates (color shading) and advective contributions (black contours) to the Eulerian heating rate  $\frac{\partial H_c}{\partial t}$ , while estimates of  $\kappa$  indicate the intensity of vertical mixing inferred from Thorpe scales in M3 data (note the log scale).

458 with  $\varepsilon < 10^{-7} \text{ W kg}^{-1}$  were sampled at nearly equidistant locations by floats M3, M6,  
 459 and M0. Conversely, overturns in the TC wake appeared more sporadically and clustered  
 460 around a few locations, but with most values of  $\varepsilon$  ranging between  $10^{-7.5}$  and  $10^{-6} \text{ W}$   
 461  $\text{kg}^{-1}$ .

## 462 5 Upper ocean thermodynamics beneath Mangkhut

### 463 5.1 Mixed layer deepening and turbulent entrainment

464 Space-time variations in subsurface  $T$  and  $S$  result from 3D advection, mixing, and  
 465 interactions with the atmosphere. In the case of intense, fast-moving TCs like Mangkhut  
 466 ( $U_{storm}/c_g \sim 2$ ), shear-driven mixing at the ML base is expected to dominate upper  
 467 ocean cooling (D'Asaro, 2003; Vincent et al., 2012). This process is evidenced by float  
 468 measurements of  $T$  averaged between 0.5 and 1.5 m depth (Fig. 11a), which show a gen-  
 469 eralized cooling trend during TC passage.

470 In particular, 1-m binned profiles of  $T$ ,  $S$  and potential density ( $\sigma_\theta$ ) from float M3  
 471 show a clear, gradual deepening of the ML base between  $x = -250$  and  $x = 0$  km (Figs.  
 472 11b-d). Successive float profiles made within  $-250 < x < 0$  km (Figs. 11b-d) show  
 473 decreases in SST but increases in both sea surface salinity (SSS) and  $\sigma_0$  as the ML deep-  
 474 ened. This corresponds to entrainment of cold, salty water from below and implies that  
 475 a fraction of turbulent kinetic energy in wind-driven currents was used to raise the po-  
 476 tential energy ( $PE$ ) of the water column. In fact, density data ( $\rho$ ) from floats M1 and

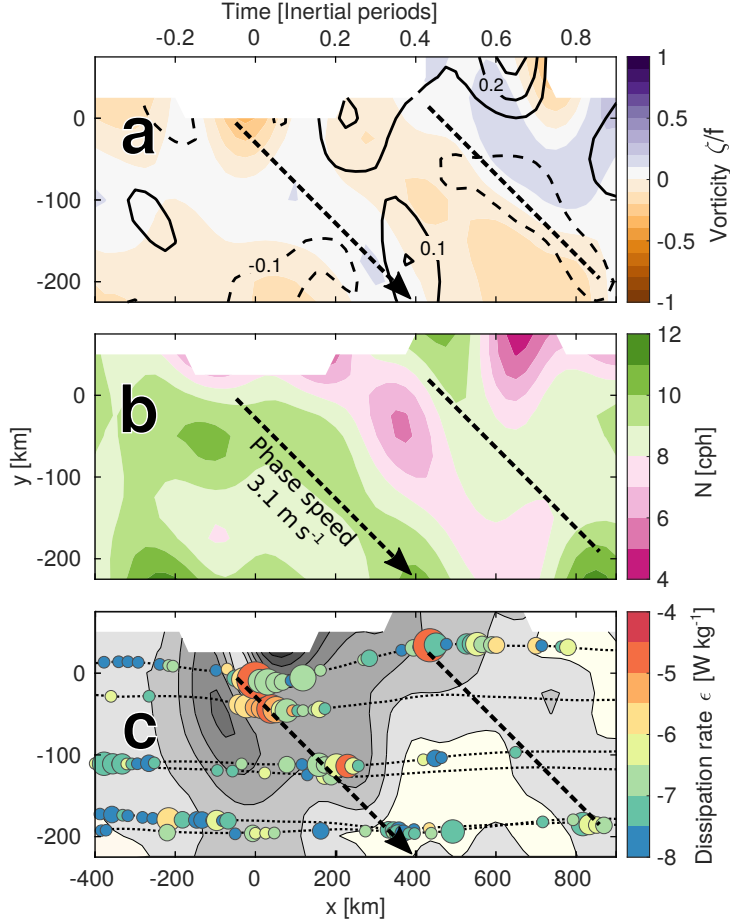


**Figure 10.** Horizontal sections of dynamical variables at 160 m depth. (a)  $\zeta^*$  (color) and  $\Gamma^*$  (black contours, negative dashed), and (b)  $N^*$ . The color of circles in panel c indicate depth-averaged estimates of  $\epsilon$ , while their size indicates the height of overturns (range is between 5 and 25 m). Gray shading in c shows  $\|\mathbf{u}_{surf}^* - \mathbf{u}_{mean}^*\|$  as a proxy for vertical shear at the mixed layer base. Thin, dotted lines denote individual float tracks. Note that scales differ in  $x$  and  $y$ .

477 M3 indicate that  $PE_{-60}^0 = \int_{-60}^0 \rho g z dz$  in the upper 60 m increased by  $\sim 9$  and  $10 \times$   
 478  $10^3 \text{ J m}^{-2}$  between  $x = -200$  and  $200$  km respectively.

479 As further evidence of the vigorous turbulence that transformed ocean thermody-  
 480 namics beneath Mangkhut, vertical profiles of  $\sigma_0$  feature  $\sim 10$  m-tall regions with unsta-  
 481 ble stratification (i.e.  $\frac{\partial \sigma_0}{\partial z} > 0$ , Fig. 11d). Thorpe scale estimates (see Section 2.2) in  
 482 Figs. 9b and 10c indicate the contribution of these density overturns to ocean turbulence.  
 483 Overall, these agree with the timing of ML deepening and SST cooling (Figs. 8c, 11a).  
 484 Quantitatively, we estimate the turbulent heat flux  $J_q \sim 4000 \text{ W m}^{-2}$  out of the ML  
 485 for float M3 near  $x = 0$  km (given  $\kappa \sim 0.1 \text{ m}^2 \text{ s}^{-1}$  and  $\frac{\partial T}{\partial z} \sim 0.01 \text{ }^\circ\text{C m}^{-1}$  in equa-  
 486 tion 5). For a ML with  $h = 40$  m, this value of  $J_q$  corresponds to an SST cooling rate  
 487  $\sim -0.1 \text{ }^\circ\text{C hr}^{-1}$ , consistent with observations in Fig. 11a. The corresponding salinity  
 488 flux  $\kappa \frac{\partial S}{\partial z}$  is  $\sim 1 \times 10^{-3} \text{ psu m s}^{-1}$  out of the ML, equivalent to a rate of increase  $\sim 0.1$   
 489  $\text{psu hr}^{-1}$ , also consistent with observations by M3 (Fig. 12a).

490 After storm passage, SSS (SST) had increased (decreased) for all floats (Figs. 11a,  
 491 12a), indicating widespread mixing of the upper ocean beneath Mangkhut. In fact, plan

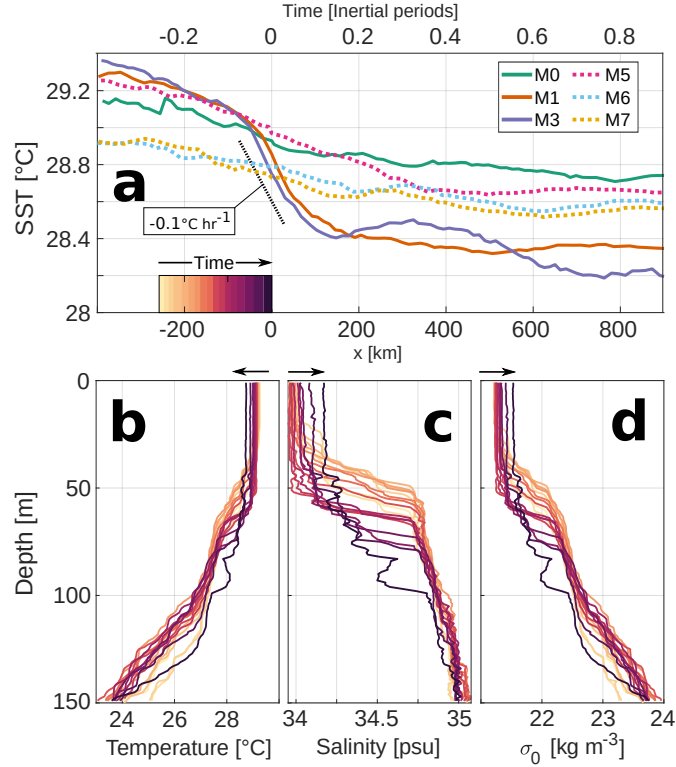


**Figure 11.** SST cooling by turbulent entrainment. (a) SST measured by all floats as a function of along-track distance  $x$ . 1-m binned profiles of (b)  $T$ , (c)  $S$ , and (d) potential density  $\sigma_0$  measured by float M3 between  $x = -250$  and  $x = 0$ . Individual profiles shown in the lower panels are color coded by their position in  $x$  (color bar in panel a).

492 views of near-surface  $T^*(x, y)$  and  $S^*(x, y)$  in Fig. 13 reveal a narrow and asymmetric  
 493 wake of cold, salty water. This indicates that SST cooling was dominated by turbulent  
 494 mixing and is consistent with greater windwork and current speeds for  $y > 0$  (Figs. 6a,  
 495 7a,b, Chang & Anthes 1978; Price 1981). Furthermore, gradients  $\frac{\partial T^*}{\partial x}$  and  $\frac{\partial S^*}{\partial t}$  (not shown)  
 496 indicate that maximum mixing rates occurred within 100 km of the TC eye, in agree-  
 497 ment with Thorpe scale estimates in Figs. 9b and 10c.

498 The impact of precipitation on SSS is opposite to that of mixing and thus can be  
 499 assessed from Fig. 12a, as floats M5, M6 and M7 sampled sharp decreases in SSS be-  
 500 tween  $x = -250$  and  $x = -150$  km. To examine the impacts of rainfall in near-surface  
 501  $T$  and  $S$ , we interpolated data from the Integrated Multi-Satellite Retrievals for Global  
 502 Precipitation Measurement (IMERG, Huffman et al. (2015)) onto the times and loca-  
 503 tions of float measurements. Estimated hourly rates of precipitation (size of circles) and  
 504 cumulative rainfall integrated since floats were at  $x = -400$  km (color) show that all  
 505 floats experienced considerable precipitation (Fig. 12b). However, and despite receiv-  
 506 ing more freshwater ( $\sim 300$  mm) than any other floats, time series of SSS from M1 and  
 507 M3 do not feature noticeable decreases attributable to precipitation (Fig. 12).

508 Why is that so? In order for precipitation to impact SSS measurements, surface  
 509 rain layers must form and remain stable for long enough ( $> 30$  minutes) to be sampled  
 510 by floats. However, this is only possible when buoyancy production by rainfall is greater  
 511 than buoyancy mixing rates that diffuse salinity gradients (E. J. Thompson et al., 2019).  
 512 Given that floats M1 and M3 were near the TC track and experienced the greatest tur-

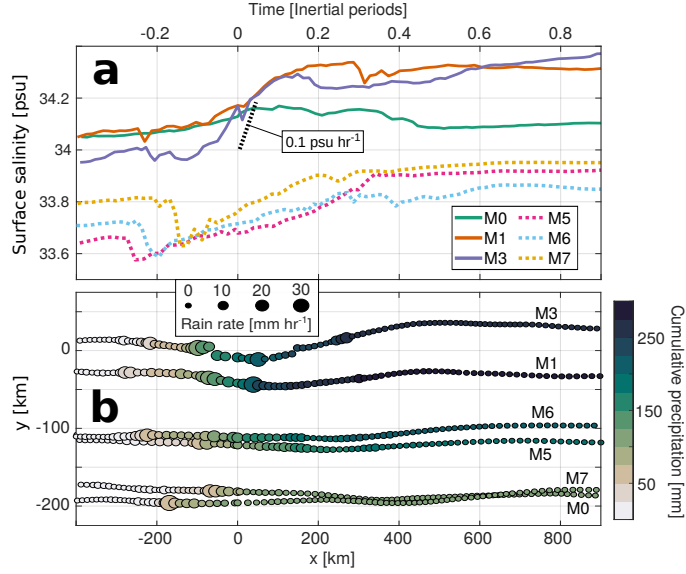


**Figure 12.** (a)  $S$  averaged in the upper 5 m along float tracks increases as a response to mixing of subsurface waters and decreases due to rainfall. (b) IMERG data show rain rates and cumulative precipitation along float trajectories.

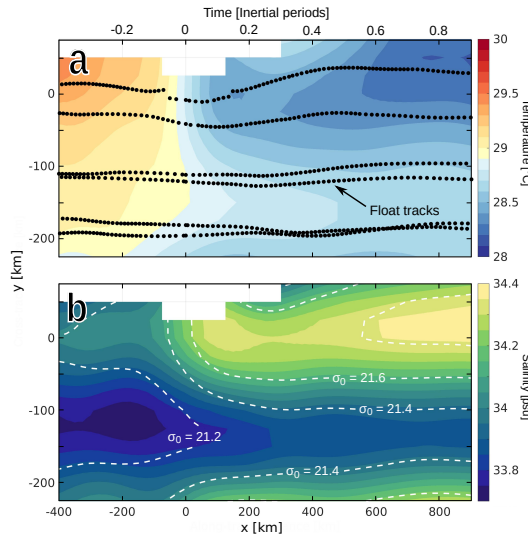


**Figure 13.** Plan view of (a)  $T^*$  and (b)  $S^*$  averaged over the upper 5 m. Black dots in Fig. 13a show the locations of each profile, while dashed contours in Fig. 13b show values of  $\sigma_\theta$  in units of  $\text{kg m}^{-3}$ .

513 bulence rates (Fig. 10c), it is likely that sudden SSS freshening by rainfall was quickly  
 514 mixed before it could be sampled.

515 In fact, successive profiles of  $T$  and  $S$  retrieved by float M7 (Fig. 14) detail the pro-  
 516 cess of rain layer formation and their subsequent destruction by turbulent mixing. Each  
 517 row of plots in this sequence shows 5 consecutive profiles spanning  $\sim 3$  h ( $\sim 75$  km).  
 518 At the beginning, float profiles ranging from  $x = -246$  to  $x = -168$  km show a well-  
 519 mixed upper ocean with no vertical gradients in  $T$  or  $S$  (Figs. 14a,b). Later on, a layer

520 of water with low  $T$  and  $S$  formed in the upper 5 m around  $x = -140$  km (black line)  
 521 but was gradually mixed and deepened over the following casts (Figs. 14c,d). This rain  
 522 layer accounts for the sharp decrease in SSS measured by M7 (Fig. 12a), while the sub-  
 523 sequent increase in SSS was consistent with mixing of cold, salty water from below. Roughly  
 524 four hours (near  $x = -50$  km) after its formation, there was little to no indication left  
 525 that a rain layer had formed around float M7 (Figs. 14e,f).

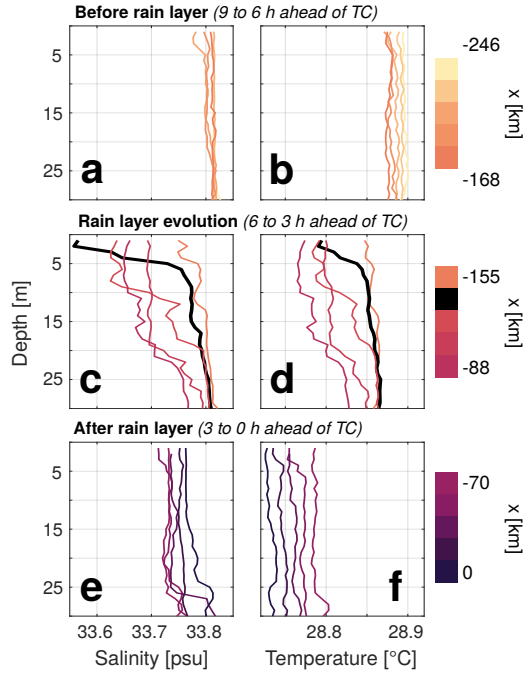


**Figure 14.** Three stages of rain layer evolution. Each row shows 5 consecutive profiles of  $T$  and  $S$  (color-coded by along-track position  $x$ ) measured by float M7 over a  $\sim 3$  h period. (a)  $S$  and (b)  $T$  before rainfall effects were noticeable. (c) and (d) show the formation of a rain layer (black line) and its gradual diffusion to greater depths. On Figs. 14e,f, turbulent mixing has mostly de-stratified the upper ocean.

526 Under fast-moving and high-intensity TCs like Mangkhut, precipitation can coun-  
 527 teract some impacts of mixing, increasing  $S$  and decreasing  $\sigma_0$  in the ML (Huang et al.,  
 528 2009; Reul et al., 2021). Mixing a rain layer with  $S = 0$  and thickness  $\Delta h_{rain} = 0.3$   
 529 m (Fig. 12b) into a ML with  $S = 34$  psu and  $h = 40$  m would decrease SSS by 0.2  
 530 psu and surface  $\sigma_0$  by  $0.15 \text{ kg m}^{-3}$ . This is equivalent to  $\sim 60\%$  of the observed increase  
 531 in SSS near the TC track (Fig. 12a) and  $\sim 25\%$  of the observed change in surface  $\sigma_0$   
 532 (Fig. 13b). In the case of Mangkhut, the SSS and surface  $\sigma_0$  anomalies induced by rain-  
 533 fall were  $\sim -30\%$  and  $\sim -15\%$  as large as those caused by mixing.

534 As an indirect effect of precipitation on air-sea interaction under TCs, we now con-  
 535 sider the energetics associated with rain layer destruction by mixing. To estimate this,  
 536 we compare  $PE$  of a water column before and after buoyancy anomalies in a rain layer  
 537  $\Delta h_{rain}$  have been mixed down to the ML base. For  $\Delta h_{rain} = 0.3$  m, PE in the upper  
 538 60 m changes by  $\sim 10^3 \text{ J m}^{-2}$ , roughly 10% of the change estimated between  $x = -200$   
 539 and  $x = 200$  km for floats M1 and M3. This suggests that rain layer destruction can  
 540 take up  $\sim 10\%$  of turbulent kinetic energy under TCs, therefore inhibiting further SST  
 541 cooling by mixing across the ML base (Jourdain et al., 2013).

542

## 5.2 Turbulent ocean heat pump

543

544

545

546

547

548

549

While the impacts of TC-driven turbulence are most noticeable in the formation of cold and salty wakes (Fig. 13), subsurface mixing helps regulate ocean heat uptake and transport (Srifer & Huber, 2007; Jansen et al., 2010; Mei et al., 2013). To assess these effects, modellers often make assumptions about the spatial and temporal extent of anomalous  $\kappa$  driven by TCs. Below, we analyze observed changes in the T-S relations to infer  $\kappa$  in the TC wake. In this way, we retrieve information about TC-driven mixing that may not be inferred from surface or ML thermodynamics alone.

550

551

552

553

554

555

556

Changes in T-S relations for floats M1 and M3 (Fig. 15a) resulted from a combination of turbulence, 3D advection, and atmospheric fluxes. However, the effects of turbulence are distinguishable from others because mixing between two water masses produces a weighted average of their original T-S properties (Hautala et al., 1996; Alford et al., 1999; Moum et al., 2003). For example, Fig. 15b, shows the average T-S relations measured by float M3 within the ranges  $200 \leq x \leq 400$  km and  $400 \leq x \leq 600$  km (dashed and solid lines respectively).

557

558

To assess the role of turbulence in setting the evolution between the two T-S profiles in Fig. 15b, we compare observations to the evolution predicted by

$$\frac{\partial T}{\partial t} \sim \kappa \frac{\partial^2 T}{\partial z^2} \quad (14)$$

$$\frac{\partial S}{\partial t} \sim \kappa \frac{\partial^2 S}{\partial z^2}. \quad (15)$$

559

560

561

562

563

564

565

566

567

568

569

Equations (14) and (15) ignore the effects of 3D advection and air-sea interaction, and thus describe only the effects of mixing on T-S relations. Taking the profile observed by M3 for  $x \in (200, 400)$  as our initial condition and setting  $\kappa = 3 \times 10^{-3}$  and  $1 \times 10^{-2} \text{ m}^2 \text{ s}^{-1}$  over 8 h (0.2 inertial periods) yields the T-S profiles shown in black dashed lines (Fig. 15b). These solutions to equations (14) and (15) agree well with the observed T-S changes for  $\sigma_\theta < 23.2 \text{ kg m}^{-3}$  but fail to explain observations at greater densities (Fig. 15b). More precisely, note that for  $\sigma_\theta > 23.5 \text{ kg m}^{-3}$ , the observed S was beyond the range of S in the initial condition. Such a transformation requires input of high-S water from elsewhere and hence cannot result from vertical mixing. Altogether, these analyses suggest mixing dominated watermass transformations down to  $\sim 110$  m depth between  $x = 200$  and  $x = 600$  km, while 3D advection had greater impacts below that.

570

571

572

573

574

575

576

577

578

Values  $\kappa > 10^{-3} \text{ m}^2 \text{ s}^{-1}$  inferred from this analysis are 3-10 times greater than the majority of Thorpe scale estimates between  $x = 200$  and 600 km, whose mean value is  $7.1 \times 10^{-4} \text{ m}^2 \text{ s}^{-1}$  (Fig. 9b). However, these estimates are not contradictory, as ocean turbulence is highly intermittent and the effective  $\kappa$  over long periods of time (Fig. 15b) is disproportionately determined by few mixing events with high  $\kappa$  (Baker & Gibson, 1987; Pearson & Fox-Kemper, 2018; Cael & Mashayek, 2021). Therefore, estimates  $\kappa$  across individual mixing events (Fig. 9b) are expected to have lower magnitudes than bulk estimates of  $\kappa$  derived from analyses of water mass transformation (Fig. 15), which yield effective or time-averaged values of  $\kappa$ .

579

580

581

582

583

584

585

586

To assess the long-term impacts of 'residual' mixing in the TC wake (Fig. 15b), we use  $\kappa = 3-10 \times 10^{-3} \text{ m}^2 \text{ s}^{-1}$  to compute  $J_q$  across the  $26^\circ\text{C}$  isotherm in  $T^*$ , yielding mean values  $\langle J_q \rangle \approx 1900 \pm 1000 \text{ W m}^{-2}$  within  $200 < x < 600$  km and  $-50 < y < 50$  km. This value of is roughly three times as large as the downwelling shortwave radiative flux in this area, which peaks near  $700 \text{ W m}^{-2}$ . Given that SST cooling typically stops only a few hours after TC passage (Figs. 11a), it is often assumed that TC-driven mixing stops then too. Nevertheless, these measurements (Fig. 15b) indicate that the vertical redistribution of heat by TC-driven turbulence can last beyond what SST data

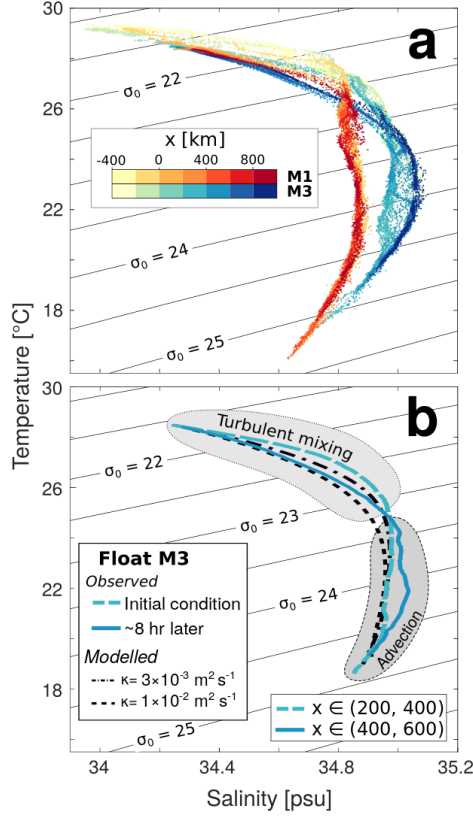


**Figure 15.**  $T$ - $S$  profiles measured by floats M1 and M3 are color-coded by along-track distance in panel **a**. Mean profiles measured between 200 and 400 km (dashed line) and between 400 and 600 km (solid line) in **b** show transformations caused throughout an 8 h period. Black dashed lines show  $T$ - $S$  properties modelled using (14) and (15) under the initial condition  $x \in (200, 400)$  km and different values of  $\kappa$ .

587 would suggest. The persistence and vertical distribution of heat content anomalies days  
 588 to weeks after Mangkhut was studied by Johnston et al. (2020), who highlighted advec-  
 589 tion of subsurface anomalies by the North Equatorial Current and potential interactions  
 590 with subsequent TCs.

## 591 6 Discussion

592 The 3D ocean response to Super Typhoon Mangkhut was reconstructed and diag-  
 593 nosed using data from profiling floats. We find general agreement between interpolated  
 594 fields and a 3D model (Figs. 6, 7). A linear model using  $\zeta$  and  $\Gamma$  instead of  $\bar{\mathbf{u}}$  to describe  
 595 ML dynamics helped interpret measurements and identify the mechanisms driving NIW  
 596 generation (Figs. 8, 9). Lastly, estimates of  $\kappa$  and  $\varepsilon$  based on  $T$  and  $S$  data provides in-  
 597 sight about the spatiotemporal persistence of TC-driven mixing and impacts to upper  
 598 ocean thermodynamics (Figs. 9b, 10c, 14, 15b).

### 599 6.1 Linear ML dynamics and inertial pumping

600 Our analyses provide a simple, yet thorough description of the mechanism respon-  
 601 sible for NIW generation by TCs because (a) for the first time, the dynamics of inertial

602 pumping are reduced to a set of ordinary differential equations (9)-(11) for  $\zeta$  and  $\Gamma$ , and  
 603 (b) observations of  $\zeta$  and  $\Gamma$  were found to be in agreement with both linear theory and  
 604 a 3D model (Figs. 6, 8). The theoretical and observational results of this study are in  
 605 close alignment with early analyses by Geisler (1970) and Price (1981, 1983), meaning  
 606 that we have not unveiled any new physics. Rather, the significance of this study is in  
 607 pointing out the inertial coupling between  $\zeta$  and  $\Gamma$  as the essence of inertial pumping and  
 608 in using observations to convincingly show those physics at work under a TC of extreme  
 609 intensity (Fig. 2c). Therefore, we hope that these analyses will be helpful to readers seek-  
 610 ing to better understand the physics of NIW generation by moving storms and improve  
 611 sampling strategies meant to observe these dynamics.

612 Past studies have inferred the 3D structure of upper ocean features powered by TCs  
 613 (Price et al., 1994; Jacob et al., 2000; Sanabia & Jayne, 2020). Here, the  $(\zeta, \Gamma)$  frame-  
 614 work presented in Section 3 helped us to unambiguously relate observed isothermal dis-  
 615 placements to TC forcing (Figs. 8, 9). This is result significant beyond the study of TCs  
 616 because it demonstrates that equations (9)-(11) can relate storm morphology (represented  
 617 by  $\nabla \times \tau$  and  $\nabla \cdot \tau$ ) to patterns in NIW generation in a 1D framework. While our re-  
 618 sults validate (9)-(11) in reproducing upwelling and NIW generation by fast-moving TCs,  
 619 future studies may test it for slow-moving TCs and frontal storms in the mid latitudes,  
 620 for which  $\nabla \cdot \tau$  may play a crucial role (see for example Kundu & Thomson 1985). Fur-  
 621 thermore, general nonlinear dynamical models based on  $\zeta$  and  $\Gamma$  (see for example Névir  
 622 & Sommer 2009) may facilitate further insight of internal waves generated by sources  
 623 other than atmospheric forcing.

## 624 6.2 Float-based estimates of $\zeta$ and $\Gamma$

625 Float estimates of  $\zeta$  and  $\Gamma$  are biased for  $x > 500$  km, as they failed to capture  
 626  $\Gamma < 0$  necessary for downwelling evidenced by  $T^*$  (Figs. 8c, 9). This is likely due to  
 627 the loss of coherence by NIWs in the TC wake, since derivatives  $\frac{\partial u^*}{\partial y}$  and  $\frac{\partial v^*}{\partial y}$  are set by  
 628 differences in measurements made more than 200 km and 12 hours apart (Figs. 1, 2).  
 629 Time-dependent biases in  $(\zeta_{surf}^*, \Gamma_{surf}^*)/f$  affect the value  $r = 0.5f$  used for numeri-  
 630 cal solutions in Fig. 8, which is considerably higher than values  $\sim 0.2f$  commonly used  
 631 to reproduce  $\bar{u}$  under extratropical storms (Pollard & Millard, 1970; D’Asaro, 1985; Al-  
 632 ford, 2001). Past studies have argued that  $r$  is greater in TC wakes due to increased NIW  
 633 energy flux divergence caused by the point-like nature of TC forcing (Kundu & Thom-  
 634 son, 1985) and interactions with background motions (Guan et al., 2014). However, afore-  
 635 mentioned uncertainties in our estimates  $(\zeta_{surf}, \Gamma_{surf})$  complicate interpretations of the  
 636 significance of the value  $r = 0.5f$  used here and its relation to NIW dynamics. A de-  
 637 tailed analysis of NIW properties using this dataset over longer timescales is given by  
 638 Johnston et al. (2021).

## 639 6.3 Float-based descriptions of mixing

640 Vertical profiles of  $T$  and  $S$  (Figs. 11, 14) detail mixing processes that modulate  
 641 storm development. Thorpe scale estimates of  $\kappa$  and  $\varepsilon$  (Figs. 9, 10) provide the spatial  
 642 distribution of mixing and potential impacts to air-sea interactions. While turbulent heat  
 643 fluxes have been calculated directly using Lagrangian instruments (D’Asaro, 2003), the  
 644 indirect approach followed here allows near real-time monitoring with potential appli-  
 645 cations in forecasting. Moreover, the watermass transformation analysis in Fig. 15 and  
 646 inferred turbulent mean heat fluxes  $J_q \approx 1900 \pm 1000$  W m<sup>-2</sup> across the 26 °C in the  
 647 TC wake show that subsurface redistribution of heat by mixing may persist after SST  
 648 stabilizes. Following these examples, future experiments may use autonomous floats to  
 649 track and explain heat anomalies induced by TCs (Johnston et al., 2020) aiming to im-  
 650 prove parameterizations used in studies of TC-climate interaction (Sriver & Huber, 2007;  
 651 Korty et al., 2008; Jansen et al., 2010).

## 7 Conclusions

Formulating the linear ML dynamics using  $\zeta$  and  $\Gamma$  in equations (9)-(11) yields a direct statement of inertial pumping and explains NIW generation behind TCs. More precisely, this gradient-based view shows that the clockwise rotation of currents rearranges  $(u, v)$  so that  $\zeta$  evolves into  $\Gamma$ , and  $\Gamma$  into  $-\zeta$  (Fig. 4). In these cycles,  $\zeta$  and  $\Gamma$  remain in quadrature as are  $u$  and  $v$  for NIWs. ML currents in observations and a 3D model of Mangkhut followed this pattern, which also controlled  $w$  in the TC wake (Figs. 6, 8).

Our analyses include multiple indirect descriptions of ocean mixing and its effects. Progressive changes in profiles of  $T$  and  $S$  indicate that SST cooling beneath Mangkhut was dominated by turbulent entrainment into the ML (Fig. 11, 13). Thorpe scale estimates in regions of unstable stratification suggest that active mixing happened ahead, under, and behind Mangkhut but was most vigorous near the TC eye (Fig. 10c), where we estimate  $\kappa \sim 10^{-1} \text{ m}^2 \text{ s}^{-1}$ . This corresponds to heat fluxes of  $\sim 4 \times 10^3 \text{ W m}^{-2}$  across the ML base (Figs. 9) and can explain the observed SST cooling rate  $\sim 0.1 \text{ }^\circ\text{C hr}^{-1}$  (Fig. 11a). Likewise, the corresponding salinity flux  $\kappa \frac{\partial S}{\partial z} \sim 2 \times 10^{-3} \text{ psu m s}^{-1}$  explains an increase of  $\sim 0.1 \text{ psu hr}^{-1}$  in SSS, roughly the same as the greatest rates in our observations (Fig. 12a). Furthermore, our measurements highlight the effects of near-surface rain layers (Fig. 14), whose diffusion into the ML was estimated to take up  $\sim 10\%$  of the turbulent kinetic energy budget near the TC track. Lastly, we documented the continued transformation of watermass characteristics hundreds of kilometers behind the TC with diffusivities  $\kappa > 10^{-3} \text{ m}^2 \text{ s}^{-1}$  down to  $\sim 110 \text{ m}$  depth (Fig. 15).

Insufficient spatial resolution in numerical models causes them to underestimate the intensity of TC winds (Walsh et al., 2007), subsequent upwelling, and NIW generation (Vincent et al., 2012). Likewise, it is unclear whether mixing parameterizations used by models can reproduce the full set of impacts reported here and others that may remain undetected. For example, accurate representation of mixing in rain layers (Fig. 14) and barrier layers (Balaguru et al., 2012; Rudzin et al., 2019) is challenging but necessary to avoid biases in forecasts of storm intensity (Hlywiak & Nolan, 2019). These and other intricacies associated with TC-driven mixing and NIW generation, including their long-term impacts on ocean thermodynamics, have yet to be comprehensively described in observations. Analyses presented in Sections 4 and 5 exemplify how data from autonomous platforms can provide insight about the multiscale ocean response to TCs. Such profiling float measurements are crucial to accurately constrain the role of TCs in global budgets of mixing and internal wave energy.

## Acknowledgments

This work is supported by grant NA17OAR4310259 from the Climate Variability and Predictability program at NOAA, and grants N00014163085 and N000141613073 from the Office of Naval Research's PISTON initiative, which are components of the international Years of the Maritime Continent program. We are grateful to the master, crew, and science party on *R/V Thomas Thompson* for their help in deploying floats. The Instrument Development Group at the Scripps Institution of Oceanography designed, prepared, and monitored the SOLO-II floats. N.G.B. is funded by Consejo Nacional de Ciencia y Tecnología (CONACyT) and UC Mexus. E.J.T. contributes effort with funding from the NOAA Weather Program Office's Precipitation Prediction Grand Challenge. Kristin Zeiden, Nathalie Zilberman, William R. Young, and three anonymous reviewers provided valuable comments.

Float data are available at the PISTON data site [www-air.larc.nasa.gov/cgi-bin/ArcView/camp2ex?TRAJECTORY=1#JOHNSTON](http://www-air.larc.nasa.gov/cgi-bin/ArcView/camp2ex?TRAJECTORY=1#JOHNSTON). SHAUN. Tropical cyclone best track data are available from the JTWC at <https://www.metoc.navy.mil/jtwc/jtwc.html?western->

701 pacific (Mangkhut was storm 26 of 2018) and coupled ocean-atmosphere model results  
 702 are available at <https://doi.org/10.5281/zenodo.4134671>.

## 703 References

- 704 Alford, M. H. (2001). Internal swell generation: The spatial distribution of energy  
 705 flux from the wind to mixed layer near-inertial motions. *Journal of Physical*  
 706 *Oceanography*, *31*(8), 2359–2368. doi: [https://doi.org/10.1175/1520-0485\(2001\)](https://doi.org/10.1175/1520-0485(2001)031<2359:ISGTSD>2.0.CO;2)  
 707 [031<2359:ISGTSD>2.0.CO;2](https://doi.org/10.1175/1520-0485(2001)031<2359:ISGTSD>2.0.CO;2)
- 708 Alford, M. H., & Gregg, M. C. (2001). Near-inertial mixing: Modulation of shear,  
 709 strain and microstructure at low latitude. *Journal of Geophysical Research:*  
 710 *Oceans*, *106*(C8), 16947–16968. doi: <https://doi.org/10.1029/2000JC000370>
- 711 Alford, M. H., Gregg, M. C., & Ilyas, M. (1999). Diapycnal mixing in the  
 712 Banda Sea: Results of the first microstructure measurements in the Indone-  
 713 sian Throughflow. *Geophysical Research Letters*, *26*(17), 2741–2744. doi:  
 714 <https://doi.org/10.1029/1999GL002337>
- 715 Asselin, O., & Young, W. R. (2020, 06). Penetration of Wind-Generated Near-  
 716 Inertial Waves into a Turbulent Ocean. *Journal of Physical Oceanography*, *50*(6),  
 717 1699–1716. Retrieved from <https://doi.org/10.1175/JPO-D-19-0319.1> doi:  
 718 <https://doi.org/10.1175/JPO-D-19-0319.1>
- 719 Baker, M. A., & Gibson, C. H. (1987). Sampling turbulence in the stratified ocean:  
 720 Statistical consequences of strong intermittency. *Journal of Physical Oceanogra-*  
 721 *phy*, *17*(10), 1817–1836. doi: [https://doi.org/10.1175/1520-0485\(1987\)017<1817:  
 722 \[STITSO>2.0.CO;2\]\(https://doi.org/10.1175/1520-0485\(1987\)017<1817:STITSO>2.0.CO;2\)](https://doi.org/10.1175/1520-0485(1987)017<1817:STITSO>2.0.CO;2)
- 723 Balaguru, K., Chang, P., Saravanan, R., Leung, L. R., Xu, Z., Li, M., & Hsieh,  
 724 J.-S. (2012). Ocean barrier layers’ effect on tropical cyclone intensification.  
 725 *Proceedings of the National Academy of Sciences*, *109*(36), 14343–14347. doi:  
 726 <https://doi.org/10.1073/pnas.1201364109>
- 727 Balmforth, N., Llewellyn Smith, S. G., & Young, W. (1998). Enhanced dispersion  
 728 of near-inertial waves in an idealized geostrophic flow. *Journal of marine research*,  
 729 *56*(1), 1–40. doi: <https://doi.org/10.1357/002224098321836091>
- 730 Cael, B., & Mashayek, A. (2021). Log-skew-normality of ocean turbulence. *Phys-*  
 731 *ical Review Letters*, *126*(22), 224502. doi: [https://doi.org/10.1103/PhysRevLett](https://doi.org/10.1103/PhysRevLett.126.224502)  
 732 [.126.224502](https://doi.org/10.1103/PhysRevLett.126.224502)
- 733 Chang, S. W., & Anthes, R. A. (1978). Numerical simulations of the ocean’s non-  
 734 linear, baroclinic response to translating hurricanes. *Journal of Physical Oceanog-*  
 735 *raphy*, *8*(3), 468–480. doi: [https://doi.org/10.1175/1520-0485\(1978\)008<0468:  
 736 \[NSOTON>2.0.CO;2\]\(https://doi.org/10.1175/1520-0485\(1978\)008<0468:NSOTON>2.0.CO;2\)](https://doi.org/10.1175/1520-0485(1978)008<0468:NSOTON>2.0.CO;2)
- 737 Chen, S. S., & Curcic, M. (2016). Ocean surface waves in Hurricane Ike (2008) and  
 738 Superstorm Sandy (2012): Coupled model predictions and observations. *Ocean*  
 739 *Modelling*, *103*, 161–176. doi: <https://doi.org/10.1016/j.ocemod.2015.08.005>
- 740 D’Asaro, E. A. (1985). The energy flux from the wind to near-inertial motions in  
 741 the surface mixed layer. *Journal of Physical Oceanography*, *15*(8), 1043–1059. doi:  
 742 [https://doi.org/10.1175/1520-0485\(1985\)015<1043:TEFFTW>2.0.CO;2](https://doi.org/10.1175/1520-0485(1985)015<1043:TEFFTW>2.0.CO;2)
- 743 D’Asaro, E. A. (1989). The decay of wind-forced mixed layer inertial oscillations due  
 744 to the  $\beta$  effect. *Journal of Geophysical Research: Oceans*, *94*(C2), 2045–2056. doi:  
 745 <https://doi.org/10.1029/JC094iC02p02045>
- 746 D’Asaro, E. A. (2003). The ocean boundary layer below Hurricane Dennis. *Jour-*  
 747 *nal of Physical Oceanography*, *33*(3), 561–579. doi: [https://doi.org/10.1175/1520-](https://doi.org/10.1175/1520-0485(2003)033<0561:TOBLBH>2.0.CO;2)  
 748 [-0485\(2003\)033<0561:TOBLBH>2.0.CO;2](https://doi.org/10.1175/1520-0485(2003)033<0561:TOBLBH>2.0.CO;2)
- 749 D’Asaro, E. A., Eriksen, C. C., Levine, M. D., Paulson, C. A., Niiler, P., &  
 750 Van Meurs, P. (1995). Upper-ocean inertial currents forced by a strong storm.  
 751 Part I: Data and comparisons with linear theory. *Journal of Physical Oceanogra-*  
 752 *phy*, *25*(11), 2909–2936. doi: [https://doi.org/10.1175/1520-0485\(1995\)025<2909:](https://doi.org/10.1175/1520-0485(1995)025<2909:)

- 753 UOICFB)2.0.CO;2
- 754 D'Asaro, E. A., Sanford, T. B., Niiler, P. P., & Terrill, E. J. (2007). Cold wake of  
755 hurricane Frances. *Geophysical Research Letters*, *34*(15). doi: [https://doi.org/10](https://doi.org/10.1029/2007GL030160)  
756 [.1029/2007GL030160](https://doi.org/10.1029/2007GL030160)
- 757 Davis, R. E. (1985). Objective mapping by least squares fitting. *Journal of*  
758 *Geophysical Research: Oceans*, *90*(C3), 4773–4777. doi: [https://doi.org/10.1029/](https://doi.org/10.1029/JC090iC03p04773)  
759 [JC090iC03p04773](https://doi.org/10.1029/JC090iC03p04773)
- 760 Davis, R. E., Sherman, J., & Dufour, J. (2001). Profiling ALACEs and other ad-  
761 vances in autonomous subsurface floats. *Journal of atmospheric and oceanic tech-*  
762 *nology*, *18*(6), 982–993. doi: [https://doi.org/10.1175/1520-0426\(2001\)018<0982:](https://doi.org/10.1175/1520-0426(2001)018<0982:)  
763 [PAAOAI\)2.0.CO;2](https://doi.org/10.1175/1520-0426(2001)018<0982:)
- 764 Ekman, V. W. (1905). On the influence of the earth's rotation on ocean-currents.
- 765 Emanuel, K. A. (1999). Thermodynamic control of hurricane intensity. *Nature*,  
766 *401*(6754), 665–669. doi: <https://doi.org/10.1038/44326>
- 767 Emanuel, K. A. (2005). Increasing destructiveness of tropical cyclones over the past  
768 30 years. *Nature*, *436*(7051), 686–688. doi: <https://doi.org/10.1038/nature03906>
- 769 Geisler, J. E. (1970). Linear theory of the response of a two layer ocean to a moving  
770 hurricane. *Geophysical and Astrophysical Fluid Dynamics*, *1*(1-2), 249–272. doi:  
771 <https://doi.org/10.1080/03091927009365774>
- 772 Gill, A. (1984). On the behavior of internal waves in the wakes of storms. *Jour-*  
773 *nal of Physical Oceanography*, *14*(7), 1129–1151. doi: [https://doi.org/10.1175/](https://doi.org/10.1175/1520-0485(1984)014(1129:OTBOIW)2.0.CO;2)  
774 [1520-0485\(1984\)014\(1129:OTBOIW\)2.0.CO;2](https://doi.org/10.1175/1520-0485(1984)014(1129:OTBOIW)2.0.CO;2)
- 775 Glenn, S., Miles, T., Seroka, G., Xu, Y., Forney, R., Yu, F., ... Kohut, J. (2016).  
776 Stratified coastal ocean interactions with tropical cyclones. *Nature Communica-*  
777 *tions*, *7*(1), 1–10. doi: <https://doi.org/10.1038/ncomms10887>
- 778 Guan, S., Zhao, W., Huthnance, J., Tian, J., & Wang, J. (2014). Observed upper  
779 ocean response to typhoon Megi (2010) in the Northern South China Sea. *Jour-*  
780 *nal of Geophysical Research: Oceans*, *119*(5), 3134–3157. doi: [https://doi.org/10](https://doi.org/10.1002/2013JC009661)  
781 [.1002/2013JC009661](https://doi.org/10.1002/2013JC009661)
- 782 Hautala, S. L., Reid, J. L., & Bray, N. (1996). The distribution and mixing of  
783 Pacific water masses in the Indonesian Seas. *Journal of Geophysical Research:*  
784 *Oceans*, *101*(C5), 12375–12389. doi: <https://doi.org/10.1029/96JC00037>
- 785 Hlywiak, J., & Nolan, D. S. (2019). The influence of oceanic barrier layers on  
786 tropical cyclone intensity as determined through idealized, coupled numer-  
787 ical simulations. *Journal of Physical Oceanography*, *49*(7), 1723–1745. doi:  
788 <https://doi.org/10.1175/JPO-D-18-0267.1>
- 789 Huang, P., Sanford, T. B., & Imberger, J. (2009). Heat and turbulent kinetic  
790 energy budgets for surface layer cooling induced by the passage of Hurricane  
791 Frances (2004). *Journal of Geophysical Research: Oceans*, *114*(C12). doi:  
792 <https://doi.org/10.1029/2009JC005603>
- 793 Huffman, G. J., Bolvin, D. T., Braithwaite, D., Hsu, K., Joyce, R., Xie, P., & Yoo,  
794 S.-H. (2015). NASA global precipitation measurement (GPM) integrated multi-  
795 satellite retrievals for GPM (IMERG). *Algorithm Theoretical Basis Document*  
796 *(ATBD) Version, 4*, 26.
- 797 Hughes, K. G., Moum, J. N., & Shroyer, E. L. (2020). Evolution of the velocity  
798 structure in the diurnal warm layer. *Journal of Physical Oceanography*, *50*(3),  
799 615–631. doi: <https://doi.org/10.1175/JPO-D-19-0207.1>
- 800 Jacob, S. D., Shay, L. K., Mariano, A. J., & Black, P. G. (2000). The 3D oceanic  
801 mixed layer response to Hurricane Gilbert. *Journal of Physical Oceanogra-*  
802 *phy*, *30*(6), 1407–1429. doi: [https://doi.org/10.1175/1520-0485\(2000\)030\(1407:](https://doi.org/10.1175/1520-0485(2000)030(1407:)  
803 [TOMLRT\)2.0.CO;2](https://doi.org/10.1175/1520-0485(2000)030(1407:)
- 804 Jansen, M. F., Ferrari, R., & Mooring, T. A. (2010). Seasonal versus permanent  
805 thermocline warming by tropical cyclones. *Geophysical Research Letters*, *37*(3).  
806 doi: <https://doi.org/10.1029/2009GL041808>

- 807 Johnson, H. L., & Garrett, C. (2004). Effects of noise on thorpe scales and run  
 808 lengths. *Journal of physical oceanography*, *34*(11), 2359–2372. doi: [https://doi](https://doi.org/10.1175/JPO3021.1)  
 809 [.org/10.1175/JPO3021.1](https://doi.org/10.1175/JPO3021.1)
- 810 Johnston, T. M. S., Chaudhuri, D., Mathur, M., Rudnick, D. L., Sengupta, D.,  
 811 Simmons, H. L., ... Venkatesan, R. (2016). Decay mechanisms of near-inertial  
 812 mixed layer oscillations in the Bay of Bengal. *Oceanography*, *29*(2), 180–191. doi:  
 813 <https://doi.org/10.5670/oceanog.2016.50>
- 814 Johnston, T. M. S., & Rudnick, D. L. (2009). Observations of the transition layer.  
 815 *Journal of Physical Oceanography*, *39*(3), 780–797. doi: [https://doi.org/10.1175/](https://doi.org/10.1175/2008JPO3824.1)  
 816 [2008JPO3824.1](https://doi.org/10.1175/2008JPO3824.1)
- 817 Johnston, T. M. S., Rudnick, D. L., Brizuela, N., & Moum, J. N. (2020). Advection  
 818 by the North Equatorial Current of a cold wake due to multiple typhoons in the  
 819 western Pacific: Measurements from a profiling float array. *Journal of Geophys-*  
 820 *ical Research: Oceans*, *125*(4), e2019JC015534. doi: [https://doi.org/10.1029/](https://doi.org/10.1029/2019JC015534)  
 821 [2019JC015534](https://doi.org/10.1029/2019JC015534)
- 822 Johnston, T. M. S., Wang, S., Lee, C.-Y., Moum, J. N., Rudnick, D. L., & Sobel, A.  
 823 (2021). Near-inertial wave propagation in the wake of Super Typhoon Mangkhut:  
 824 Measurements from a profiling float array. *Journal of Geophysical Research:*  
 825 *Oceans*, e2020JC016749. doi: <https://doi.org/10.1029/2020JC016749>
- 826 Jourdain, N. C., Lengaigne, M., Vialard, J., Madec, G., Menkès, C. E., Vincent,  
 827 E. M., ... Barnier, B. (2013). Observation-based estimates of surface cooling  
 828 inhibition by heavy rainfall under tropical cyclones. *Journal of Physical Oceanog-*  
 829 *raphy*, *43*(1), 205–221. doi: <https://doi.org/10.1175/JPO-D-12-085.1>
- 830 Korty, R. L., Emanuel, K. A., & Scott, J. R. (2008). Tropical cyclone-induced  
 831 upper-ocean mixing and climate: Application to equable climates. *Journal of Cli-*  
 832 *mate*, *21*(4), 638–654. doi: <https://doi.org/10.1175/2007JCLI1659.1>
- 833 Kundu, P. K., & Thomson, R. E. (1985). Inertial oscillations due to a moving  
 834 front. *Journal of Physical Oceanography*, *15*(8), 1076–1084. doi: [https://doi.org/](https://doi.org/10.1175/1520-0485(1985)015(1076:IODTAM)2.0.CO;2)  
 835 [10.1175/1520-0485\(1985\)015\(1076:IODTAM\)2.0.CO;2](https://doi.org/10.1175/1520-0485(1985)015(1076:IODTAM)2.0.CO;2)
- 836 Kunze, E. (1985). Near-inertial wave propagation in geostrophic shear. *Jour-*  
 837 *nal of Physical Oceanography*, *15*(5), 544–565. doi: [https://doi.org/10.1175/1520-](https://doi.org/10.1175/1520-0485(1985)015(0544:NIWPIG)2.0.CO;2)  
 838 [0485\(1985\)015\(0544:NIWPIG\)2.0.CO;2](https://doi.org/10.1175/1520-0485(1985)015(0544:NIWPIG)2.0.CO;2)
- 839 Le Traon, P., Nadal, F., & Ducet, N. (1998). An improved mapping method  
 840 of multisatellite altimeter data. *Journal of atmospheric and oceanic technol-*  
 841 *ogy*, *15*(2), 522–534. doi: [https://doi.org/10.1175/1520-0426\(1998\)015\(0522:](https://doi.org/10.1175/1520-0426(1998)015(0522:AIMMOM)2.0.CO;2)  
 842 [AIMMOM\)2.0.CO;2](https://doi.org/10.1175/1520-0426(1998)015(0522:AIMMOM)2.0.CO;2)
- 843 Mater, B. D., Venayagamoorthy, S. K., St. Laurent, L., & Moum, J. N. (2015). Bi-  
 844 ases in Thorpe-scale estimates of turbulence dissipation. Part I: Assessments from  
 845 large-scale overturns in oceanographic data. *Journal of Physical Oceanography*,  
 846 *45*(10), 2497–2521. doi: <https://doi.org/10.1175/JPO-D-14-0128.1>
- 847 Mei, W., Primeau, F., McWilliams, J. C., & Pasquero, C. (2013). Sea surface height  
 848 evidence for long-term warming effects of tropical cyclones on the ocean. *Proceed-*  
 849 *ings of the National Academy of Sciences*, *110*(38), 15207–15210. doi: [https://doi](https://doi.org/10.1073/pnas.1306753110)  
 850 [.org/10.1073/pnas.1306753110](https://doi.org/10.1073/pnas.1306753110)
- 851 Moum, J., Farmer, D., Smyth, W., Armi, L., & Vagle, S. (2003). Structure and  
 852 generation of turbulence at interfaces strained by internal solitary waves prop-  
 853 agating shoreward over the continental shelf. *Journal of Physical Oceanogra-*  
 854 *phy*, *33*(10), 2093–2112. doi: [https://doi.org/10.1175/1520-0485\(2003\)033\(2093:](https://doi.org/10.1175/1520-0485(2003)033(2093:SAGOTA)2.0.CO;2)  
 855 [SAGOTA\)2.0.CO;2](https://doi.org/10.1175/1520-0485(2003)033(2093:SAGOTA)2.0.CO;2)
- 856 Nagai, T., Tandon, A., Kunze, E., & Mahadevan, A. (2015). Spontaneous genera-  
 857 tion of near-inertial waves by the Kuroshio Front. *Journal of Physical Oceanogra-*  
 858 *phy*, *45*(9), 2381–2406. doi: <https://doi.org/10.1175/JPO-D-14-0086.1>
- 859 Névir, P., & Sommer, M. (2009). Energy–vorticity theory of ideal fluid mechan-  
 860 ics. *Journal of the Atmospheric Sciences*, *66*(7), 2073–2084. doi: <https://doi.org/>

- 10.1175/2008JAS2897.1
- 861 Nilsson, J. (1995, 04). Energy flux from traveling hurricanes to the oceanic inter-  
 862 nal wave field. *Journal of Physical Oceanography*, 25(4), 558–573. doi: [https://doi](https://doi.org/10.1175/1520-0485(1995)025<0558:EFFTHT>2.0.CO;2)  
 863 .org/10.1175/1520-0485(1995)025<0558:EFFTHT>2.0.CO;2
- 864 Osborn, T. (1980). Estimates of the local rate of vertical diffusion from dissipation  
 865 measurements. *Journal of physical oceanography*, 10(1), 83–89. doi: [https://doi](https://doi.org/10.1175/1520-0485(1980)010<0083:EOTLRO>2.0.CO;2)  
 866 .org/10.1175/1520-0485(1980)010<0083:EOTLRO>2.0.CO;2
- 867 Pearson, B., & Fox-Kemper, B. (2018). Log-normal turbulence dissipation in global  
 868 ocean models. *Physical review letters*, 120(9), 094501. doi: [https://doi.org/10](https://doi.org/10.1103/PhysRevLett.120.094501)  
 869 .1103/PhysRevLett.120.094501
- 870 Pollard, R. T., & Millard, R. (1970). Comparison between observed and sim-  
 871 ulated wind-generated inertial oscillations. In *Deep sea research and oceanog-*  
 872 *raphic abstracts* (Vol. 17, pp. 813–821). doi: [https://doi.org/10.1016/](https://doi.org/10.1016/0011-7471(70)90043-4)  
 873 0011-7471(70)90043-4
- 874 Pollard, R. T., Rhines, P. B., & Thompson, R. O. (1973). The deepening of the  
 875 wind-mixed layer. *Geophysical Fluid Dynamics*, 4(4), 381–404. doi: [https://doi](https://doi.org/10.1080/03091927208236105)  
 876 .org/10.1080/03091927208236105
- 877 Price, J. F. (1981). Upper ocean response to a hurricane. *Journal of Physi-*  
 878 *cal Oceanography*, 11(2), 153–175. doi: [https://doi.org/10.1175/1520-0485\(1981\)](https://doi.org/10.1175/1520-0485(1981)011<0153:UORTAH>2.0.CO;2)  
 879 011<0153:UORTAH>2.0.CO;2
- 880 Price, J. F. (1983). Internal wave wake of a moving storm. Part I. Scales, energy  
 881 budget and observations. *Journal of Physical Oceanography*, 13(6), 949–965. doi:  
 882 [https://doi.org/10.1175/1520-0485\(1983\)013<0949:IWWOAM>2.0.CO;2](https://doi.org/10.1175/1520-0485(1983)013<0949:IWWOAM>2.0.CO;2)
- 883 Price, J. F., Sanford, T. B., & Forristall, G. Z. (1994). Forced stage response to  
 884 a moving hurricane. *Journal of Physical Oceanography*, 24(2), 233–260. doi:  
 885 [https://doi.org/10.1175/1520-0485\(1994\)024<0233:FSRTAM>2.0.CO;2](https://doi.org/10.1175/1520-0485(1994)024<0233:FSRTAM>2.0.CO;2)
- 886 Reul, N., Chapron, B., Grodsky, S. A., Guimbard, S., Kudryavtsev, V., Foltz, G. R.,  
 887 & Balaguru, K. (2021). Satellite observations of the sea surface salinity response  
 888 to tropical cyclones. *Geophysical research letters*, 48(1), e2020GL091478. doi:  
 889 <https://doi.org/10.1029/2020GL091478>
- 890 Rudzin, J. E., Shay, L. K., & Jaimes de la Cruz, B. (2019). The impact of the  
 891 Amazon–Orinoco River plume on enthalpy flux and air–sea interaction within  
 892 Caribbean Sea tropical cyclones. *Monthly Weather Review*, 147(3), 931–950. doi:  
 893 <https://doi.org/10.1175/MWR-D-18-0295.1>
- 894 Sanabia, E. R., & Jayne, S. R. (2020). Ocean observations under two major hur-  
 895 ricanes: Evolution of the response across the storm wakes. *AGU Advances*, 1(3),  
 896 e2019AV000161. doi: <https://doi.org/10.1029/2019AV000161>
- 897 Sanford, T. B., Price, J. F., & Garton, J. B. (2011). Upper-ocean response to Hur-  
 898 ricane Frances (2004) observed by profiling EM-APEX floats. *Journal of Physical*  
 899 *Oceanography*, 41(6), 1041–1056. doi: <https://doi.org/10.1175/2010JPO4313.1>
- 900 Scotti, A. (2015). Biases in Thorpe-scale estimates of turbulence dissipation. Part II:  
 901 Energetics arguments and turbulence simulations. *Journal of Physical Oceanogra-*  
 902 *phy*, 45(10), 2522–2543. doi: <https://doi.org/10.1175/JPO-D-14-0092.1>
- 903 Shay, L. K., & Chang, S. W. (1997). Free surface effects on the near-inertial  
 904 ocean current response to a hurricane: A revisit. *Journal of Physical Oceanog-*  
 905 *raphy*, 27(1), 23–39. doi: [https://doi.org/10.1175/1520-0485\(1990\)020<1405:](https://doi.org/10.1175/1520-0485(1990)020<1405:FSEOTN>2.0.CO;2)  
 906 FSEOTN>2.0.CO;2
- 907 Shay, L. K., Elsberry, R. L., & Black, P. G. (1989). Vertical structure of the ocean  
 908 current response to a hurricane. *Journal of Physical Oceanography*, 19(5), 649–  
 909 669. doi: [https://doi.org/10.1175/1520-0485\(1989\)019<0649:VSOTOC>2.0.CO;2](https://doi.org/10.1175/1520-0485(1989)019<0649:VSOTOC>2.0.CO;2)
- 910 Skamarock, W. C., Klemp, J. B., Dudhia, J., Gill, D. O., Barker, D. M., Wang, W.,  
 911 & Powers, J. G. (2008). A description of the Advanced Research WRF version 3.  
 912 NCAR Technical note-475+ STR.
- 913 Sriver, R. L., & Huber, M. (2007). Observational evidence for an ocean heat pump
- 914

- 915 induced by tropical cyclones. *Nature*, 447(7144), 577–580. doi: <https://doi.org/10.1038/nature05785>
- 916
- 917 Thomas, L. N., Rainville, L., Asselin, O., Young, W. R., Girton, J., Whalen, C. B.,  
 918 ... Hormann, V. (2020). Direct observations of near-inertial wave  $\zeta$ -refraction  
 919 in a dipole vortex. *Geophysical Research Letters*, 47(21), e2020GL090375. doi:  
 920 <https://doi.org/10.1029/2020GL090375>
- 921 Thompson, A., Gille, S. T., MacKinnon, J. A., & Sprintall, J. (2007). Spatial and  
 922 temporal patterns of small-scale mixing in Drake Passage. *Journal of Physical*  
 923 *Oceanography*, 37(3), 572–592. doi: <https://doi.org/10.1175/JPO3021.1>
- 924 Thompson, E. J., Moum, J. N., Fairall, C. W., & Rutledge, S. A. (2019). Wind  
 925 limits on rain layers and diurnal warm layers. *Journal of Geophysical Research:*  
 926 *Oceans*, 124(2), 897–924. doi: <https://doi.org/10.1029/2018JC014130>
- 927 Thorpe, S. (1977). Turbulence and mixing in a Scottish loch. *Philosophical Trans-*  
 928 *actions of the Royal Society of London. Series A, Mathematical and Physical*  
 929 *Sciences*, 286(1334), 125–181. doi: <https://doi.org/10.1098/rsta.1977.0112>
- 930 Turner, J., & Kraus, E. (1967). A one-dimensional model of the seasonal thermo-  
 931 cline i. a laboratory experiment and its interpretation. *Tellus*, 19(1), 88–97. doi:  
 932 <https://doi.org/10.1111/j.2153-3490.1967.tb01461.x>
- 933 Vincent, E. M., Lengaigne, M., Madec, G., Vialard, J., Samson, G., Jourdain, N. C.,  
 934 ... Jullien, S. (2012). Processes setting the characteristics of sea surface cooling  
 935 induced by tropical cyclones. *Journal of Geophysical Research: Oceans*, 117(C2).  
 936 doi: <https://doi.org/10.1029/2011JC007396>
- 937 Wallcraft, A., Metzger, E., & Carroll, S. (2009). *Software design description for*  
 938 *the hybrid coordinate ocean model (HYCOM), Version 2.2* (Tech. Rep.). Naval Re-  
 939 search Lan Stennis Space Center MS Oceanography Div.
- 940 Walsh, K., Fiorino, M., Landsea, C., & McInnes, K. (2007). Objectively deter-  
 941 mined resolution-dependent threshold criteria for the detection of tropical cyclones  
 942 in climate models and reanalyses. *Journal of Climate*, 20(10), 2307–2314. doi:  
 943 <https://doi.org/10.1175/JCLI4074.1>
- 944 Wamsley, L. (2018, Sep). Dozens more feared dead in the philippines after typhoon  
 945 triggers mudslide. *National Public Radio*. Retrieved from [https://www.npr.org/](https://www.npr.org/2018/09/17/648866035/dozens-more-feared-dead-in-the-philippines-after-typhoon-triggers-mudslide)  
 946 [2018/09/17/648866035/dozens-more-feared-dead-in-the-philippines-after](https://www.npr.org/2018/09/17/648866035/dozens-more-feared-dead-in-the-philippines-after-typhoon-triggers-mudslide)  
 947 [-typhoon-triggers-mudslide](https://www.npr.org/2018/09/17/648866035/dozens-more-feared-dead-in-the-philippines-after-typhoon-triggers-mudslide)
- 948 Whitt, D. B., & Thomas, L. N. (2015). Resonant generation and energetics of wind-  
 949 forced near-inertial motions in a geostrophic flow. *Journal of Physical Oceanogra-*  
 950 *phy*, 45(1), 181–208. doi: <https://doi.org/10.1175/JPO-D-14-0168.1>
- 951 Zweers, N., Makin, V., De Vries, J., & Burgers, G. (2010). A sea drag relation for  
 952 hurricane wind speeds. *Geophysical Research Letters*, 37(21). doi: [https://doi.org/](https://doi.org/10.1029/2010GL045002)  
 953 [10.1029/2010GL045002](https://doi.org/10.1029/2010GL045002)